



Ca-Cu/Al₂O₃ catalysts for H₂S removal at near ambient temperature: Synthesis, characterization, DFT calculation, and mechanistic insights

Mengxue Yin^{a,b,1}, Wenqing Zhang^{a,1}, Suresh C. Pillai^{d,e}, Hailong Wang^{f,g}, Hongliang Yin^a, Zhihao Wu^{a,b}, Yan Zheng^a, Long Zhao^a, Feiyue Fan^{c,*}, Hong Hou^{a,*}

^a State Key Laboratory of Environmental Criteria and Risk Assessment, Chinese Research Academy of Environmental Sciences, Beijing 100012, China

^b College of Water Sciences, Beijing Normal University, Beijing 100875, China

^c Technical Centre for Soil, Agriculture and Rural Ecology and Environment, Ministry of Ecology and Environment, Beijing 100012, China

^d Nanotechnology Research Group, Department of Environmental Science, Atlantic Technological University, ATU Sligo, Ash Lane, Sligo F91 YW50, Ireland

^e Health and Biomedical Research Centre (HEAL), Atlantic Technological University, ATU Sligo, Ash Lane, Sligo F91 YW50, Ireland

^f School of Environmental and Chemical Engineering, Foshan University, Guangdong, Foshan 528000, China

^g Guangdong Provincial Key Laboratory of Integrated Agro-environmental Pollution Control and Management, Institute of Eco-environmental and Soil Sciences, Guangdong Academy of Sciences, Guangzhou 510650, China

ARTICLE INFO

Keywords:

Catalytic oxidation

Hydrogen sulfide

Ca-Cu/Al₂O₃ catalyst

Synergistic catalytic mechanism

Sulfur recovery

ABSTRACT

A series of Ca-doped Cu_xO/Al₂O₃ catalysts were developed using the excessive impregnation method for H₂S catalytic oxidation at near-ambient temperatures. Ca(NO₃)-Cu_xO/Al₂O₃ catalyst with 2.5 wt% Ca exhibited optimal H₂S desulfurization performance at 60 °C and RH 60%, achieving an H₂S removal capacity of 401.34 mg/g. Experimental, characterization, and DFT calculation results demonstrate that during the catalytic oxidation of H₂S, H₂O can be catalytically convert into ·OH while simultaneously capturing and dissociating H₂S. The ·OH and NO₃ then catalyze the oxidation of HS⁻/S²⁻ to elemental S. Moreover, the redundant OH adsorbed on the basic sites can buffer the pH and promote the dissociation of H₂S. The above cyclic process could alleviate the deactivation of the Ca-Cu/Al₂O₃ catalyst. Therefore, a ·OH-induced desulfurization mechanism assisted with Ca²⁺ buffer the pH and NO₃ cyclic oxidation of H₂S has been proposed. This work contributes to the preparation of high-capacity mental-based catalysts for H₂S oxidation.

1. Introduction

As a colorless, corrosive, and highly toxic gas with a distinctive odor reminiscent of rotten eggs, hydrogen sulfide (H₂S) is prevalent in numerous chemical processes, landfills, and shale gas formations, permeating diverse environments. [1,2]. H₂S has the potential to corrode transportation pipelines and buildings, contribute to the formation of acid rain in the atmosphere, degrade the environment, and pose health risks to humans [3,4]. With a remarkably low olfactory threshold of 0.0008 mg/m³, even at low concentrations, H₂S can cause discomfort. Therefore, reducing H₂S emission levels below the olfactory threshold is crucial to minimize its influence on the environment and human health [5].

Under appropriate conditions, selective catalytic oxidation (SCO) offers a highly effective means of completely converting H₂S into sulfur.

This makes it particularly suitable for the efficient and thorough removal of H₂S, thereby establishing SCO as a hot topic [1,6,7]. SCO technology can be categorized into two classes, taking into account the reaction temperature about the sulfur dew point (approximately 180 °C): high-temperature (> 180 °C) H₂S-SCO technology and low-temperature (< 180 °C) H₂S-SCO technology. The high-temperature H₂S-SCO technology, primarily based on the Claus process, can achieve desulfurization efficiencies of only 99.2–99.5%, even under the most stringent conditions [7–9]. The sulfur converted from H₂S can also oxidize into SO₂, causing secondary pollution [7]. Therefore, the high-temperature H₂S-SCO technology is unsuitable for locations that do not meet the thermodynamic requirements and residential areas with strict H₂S treatment regulations. In the low-temperature H₂S-SCO process, sulfur condenses and is stored within the catalyst's pore structure, achieving a 100% removal rate of H₂S [7,10,11]. This technology is

* Corresponding authors.

E-mail addresses: fanfeiyue28@163.com (F. Fan), honghou@craes.org.cn (H. Hou).

¹ These authors contributed to the work equally and should be regarded as co-first authors.

suitable for situations with no thermodynamic conditions and strict requirements for H₂S treatment. The core of this technology lies in the catalyst used.

Metal oxides are the main active phases for H₂S desulfurization, such as the oxides of Ag, Cu, Zn, Co, Ni, Ca, Mg, V, and Sn [12–16]. Among the various metal oxides, copper is widely employed in catalysis owing to its high activity and cost-effectiveness. In particular, CuO demonstrates exceptional catalytic performance for H₂S and finds widespread use in low-temperature H₂S-SCO processes. Due to its large particle size, inadequate specific surface area (SSA), and limited micro- and meso-pores, the single-metal oxide (MO) exhibits a low H₂S removal efficiency. Researchers have developed a solution to overcome these challenges by dispersing MOs onto highly porous supports, thereby reducing particle size [13,17–22]. This approach increases the SSA, improves metal stability, and enhances the H₂S removal. Supporting Cu_xO on γ -Al₂O₃ is reported to significantly enhance its H₂S desulfurization performance [23]. This is attributed to the large SSA, pore volume, and hydrophilicity of γ -Al₂O₃, which significantly improve the H₂S desulfurization performance of Cu_xO. Furthermore, the H₂S desulfurization performance is further enhanced by doping a second component [23,24].

It has been reported that the desulfurization performance of a catalyst can be improved by its surface basicity or the presence of basicity groups. Introducing a basic metal into the catalyst is an effective method to increase its surface basicity. Commonly used alkaline impregnating solutions include Na₂CO₃, NaOH, K₂CO₃, KOH, and Mg(NO₃)₂ [25–27]. Researchers have discovered that alkaline earth Mg performed better performance than conventional alkaline salts [25]. Calcium (Ca), also an alkaline earth metal, is widely used as a desulfurizing agent for hot flue gas SO₂ removal due to its lower cost and environmental friendliness [28]. Recently, excellent desulfurization performance has been achieved by supporting CaO on activated carbon in the low-temperature H₂S-SCO process [29]. Moreover, it has been found that the low reactivity adsorption of H₂S by Ca prevents its conversion into sulfides, thus slowing down catalyst deactivation [24]. Additionally, the high alkalinity of Ca facilitates the dissociation of H₂S [30]. Therefore, it is reasonable to enhance the desulfurization performance of Cu_xO/ γ -Al₂O₃ by utilizing the high alkalinity of Ca, especially by exploiting the oxidizing property of NO₃ in alkali metal nitrates. By combining the advantages of Cu_xO/ γ -Al₂O₃ with the prominent characteristics of Ca²⁺ and NO₃⁻, it is expected to develop an ideal catalyst. Previous studies have mainly focused on using single or multiple metal oxides as active components for H₂S removal [3,10,15,17,18,20–24]. The simultaneous utilization of nitrates and metal oxides as active components for low-temperature H₂S removal was rarely reported. Moreover, the understanding of the reaction mechanism is still unknown, which hampers the rational application and optimization of metal-based catalysts.

In this study, the objective was to develop efficient and stable catalysts for the low-temperature H₂S-SCO process. To achieve this, a group of Ca(NO₃)₂-Cu_xO/Al₂O₃ catalysts with different loadings of Ca were prepared. The performance of these catalysts in H₂S removal was examined under various humidity and temperature. The catalysts were comprehensively characterized before and after H₂S removal, and DFT calculations were employed to propose potential desulfurization mechanisms. This catalyst shows promise as an effective solution for low-temperature H₂S removal.

2. Experimental

2.1. Materials

Activated alumina (γ -Al₂O₃), calcium nitrate hydrate (Ca(NO₃)₂·H₂O) and copper nitrate hexahydrate (Cu(NO₃)₂·3 H₂O), and were obtained from China National Medicines Co., LTD, all of which were analytical grade.

2.2. Catalyst preparation

Al₂O₃ supported with a Ca-Cu composite was synthesized using the excessive impregnation method. After determining the superior H₂S removal performance, Cu_xO/Al₂O₃ (3 wt%) was chosen. The preparation procedure is described as follows: impregnate 5 g of γ -Al₂O₃ particles with a size range of 380–830 μ m in 20 mL of Cu(NO₃)₂ solution with a concentration of 0.776 mol/L, followed by 30 min of ultrasound treatment, and continue the immersion at rest for 11.5 h. The wet catalyst was then dried in an oven for 30 min at 60 °C. Subsequently, the catalysts were heated at a heating rate of 5 °C/min until reaching a temperature of 500 °C in a muffle furnace. Then it was calcined for 4 h under atmospheric conditions at 500 °C.

To further study the influence of Ca-compound on the H₂S desulfurization performance, Ca/Al₂O₃ samples were also synthesized. The preparation procedure for the Ca/Al₂O₃ catalyst, which contained 2.5 wt% Ca²⁺, was as follows: Initially, 5 g of γ -Al₂O₃ were immersed in a 20 mL solution containing 3.59 g of Ca(NO₃)₂·H₂O. The subsequent impregnation, drying, and calcination steps were identical to those used to prepare the Cu_xO/Al₂O₃ catalyst.

The Ca content optimization was performed based on the previously prepared Cu_xO/Al₂O₃ catalyst (3 wt%). We utilized a sequential impregnation technique to prepare the Ca-Cu_xO/Al₂O₃ catalysts. Ca(NO₃)₂·4 H₂O weighing 0.51 g, 1.54 g, 2.56 g, 3.59 g, and 4.61 g was dissolved in 20 mL of distilled water to obtain a Ca(NO₃)₂ solution. The Ca(NO₃)₂ solution was then used to prepare Ca-Cu_xO/Al₂O₃ catalysts with corresponding Ca/catalyst ratios of 1 wt%, 1.5 wt%, 2 wt%, 2.5 wt%, and 3 wt%, respectively. The subsequent steps of impregnation, drying, and calcination followed the same procedure as the preparation steps for Cu_xO/Al₂O₃. Quantification of Ca was achieved through the use of inductively coupled plasma-optical emission spectrometry (ICP-OES, Optima5300DV).

2.3. Performance tests

Dynamic H₂S removal tests were conducted using a fixed bed adsorber under atmospheric pressure conditions. Specifically, 1 g of catalyst was placed in an acrylic tube with an inner diameter of 14 mm. Prior to the test, the catalyst was prewetted for 30 min at a flow rate of 120 mL/min. The prewetted catalyst was then exposed to a mixed gas stream in a reactor, comprising moisture-containing air and H₂S/N₂, flowing at a total rate of 150 mL/min. The initial H₂S concentration in the system was measured at 1390 \pm 76 mg/m³. A mass flow controller (Sevenstar CS100) regulated the gas flow rate. The gas humidity (RH 0–80%) and reaction temperature (40–70 °C) were regulated separately using a steam generator and a temperature controller. The concentration of H₂S was determined using a Shimadzu GC2010 chromatograph equipped with a flame photometric detector (FPD). Fig. S1 illustrates the test device utilized. The data was recorded through at least three measurements, with an error range not exceeding 5% to ensure experiment repeatability.

The test was concluded when the H₂S concentration reached 76 mg/m³ at the outlet. The catalyst's performance was assessed by determining its breakthrough sulfur capacity (S_c, mg H₂S/g catalyst). This capacity was calculated using the following equation:

$$S_c = \frac{M * u * \left(\int_0^t (c_{in} - c_{out}) dt \right)}{10^6 * V_{mol} * m} \quad (1)$$

Where: *M* is the molecular mass of H₂S (34 g/mol), *u* is the flow rate of the H₂S/N₂ mixed gas (150 mL/min in this study), *c_{in}* and *c_{out}* are the H₂S concentrations at the inlet and outlet, respectively (1390 and 76 mg/m³ respectively in this study), *t* is the time taken to reach 76 mg/m³ (min). *V_{mol}* is the molar volume of gas (22.4 L/mol at standard conditions). *m* is the mass of the catalyst in the reactor (1 g in this study).

2.4. Sulfur recovery experiment

The sulfur recovery experiment was conducted in a vertical tubular furnace (Fig. S2). The specific operating procedures and test devices are shown in the [supplementary material](#).

2.5. Characterization

To examine the pore structure, the N₂ adsorption-desorption isotherms of the samples were measured at −195.8 °C using a TRISTAR II 3020 M instrument. The sample's surface area was determined using the standardized Brunauer-Emmett-Teller (BET) method, while the pore volume was calculated using the Barrett-Joyner-Halenda (BJH) method. Scanning electron microscope (SEM) and energy dispersive X-ray (EDX) images were obtained using a Hitachi SU-8010 instrument to examine the catalyst's surface morphology and element distribution. To analyze the crystal structure of the catalyst, X-ray diffraction (XRD) was performed using a SmartLab smart X-ray diffractometer, with diffraction angles tested in the range of 10–80°. X-ray photoelectron spectroscopy (XPS) was performed using a PHI Quantera SXM spectrometer to assess the chemical states of surface elements. The microstructure was examined using a JEOL JEM-F200 transmission electron microscope (TEM) apparatus from Japan. Fourier transform infrared (FTIR) spectra were acquired using an X70 combined thermal analysis system from Netzsch, Germany to investigate the presence of functional groups on the catalyst surface. The Netzsch STA2500 instrument was utilized to conduct thermogravimetric analysis-derivative thermogravimetry (TG-DTG) testing for detecting weight loss of the samples with increasing temperature. The catalysts' CO₂ temperature-programmed desorption (CO₂-TPD) was performed on an AUTO CHEM 2920 instrument. The surface defect and hydroxyl radicals (·OH) analysis were examined using electron paramagnetic resonance (EPR) analysis conducted on a Bruker EMXPLUS spectrometer. To assess the catalysts' ability to generate ·OH, a DMPO aqueous suspension was utilized as the capturing agent.

2.6. Computational method

The Vienna Ab-initio Simulation Package (VASP) was used to conduct Density Functional Theory (DFT) calculations utilizing the generalized gradient approximation (GGA) and applying the Perdew–Burke–Ernzerho (PBE) formulation [31,32]. To describe the valence electrons and elucidate the characteristics of the ionic nuclei, we employed the method of using projected augmented wave (PAW) potentials in combination with a basis set consisting of plane waves. A specific cutoff energy of 520 eV [33,34] was chosen for this purpose. To accommodate partial occupancies of the Kohn-Sham orbitals, we implemented the Gaussian smearing method with a smearing width of 0.05 eV. The self-consistency of the electronic energy was established when the energy variation fell below 10^{−5} eV. To attain convergence in the geometry optimization process, we set the threshold for force change at a value lower than 0.05 eV/Å. To account for dispersion interactions, Grimme's DFT-D3 methodology [35] was incorporated. Following this, a surface model was constructed, possessing periodicity in both the x and y directions, and an independent periodicity in the z direction. To isolate the surface slab from its periodic replicas, we introduced a vacuum layer with a thickness of 18 Å.

The equilibrium lattice constants of CuO, Cu₂O, and Ca(NO₃)₂ unit cells were optimized. These were then used to construct a CuO, Cu₂O, Ca(NO₃)₂ (110) surface model. In order to optimize the structure, a 3×3×1 k-point grid was utilized for k-point sampling within the Brillouin zone. The bottom two atomic layers remained fixed during this process, while the top two layers were allowed to relax. The Cu₂O-CuO structures were established using the Cu₂O surface and CuO surface with the lattice parameters (a=18.1566 Å, b=13.4678 Å, c=28.8571 Å). The Cu₂O-CuO structures with 6 layers of Cu-O-Cu layers included 172 atoms. Similarly, in the context of structural optimizations, a k-point grid of 3×3×1 was

implemented to sample the Brillouin zone and ensure accuracy. In this process, the bottom two atomic layers were held fixed, while relaxation was permitted for the top two layers (Fig. S3). CuO-Cu₂O-Ca(NO₃)₂ structures were established using the Cu₂O surface, CuO surface, and Ca(NO₃)₂ surface with the lattice parameters (a=18.9361 Å, b=13.5183 Å, c=28.8571 Å) (Fig. S4).

During structural optimizations, we sampled the Brillouin zone at the Γ point for k-point sampling, enabling all atoms to relax. Using the equation (Eq. 2), the calculation was performed to determine the free energy of H₂S on the surface or that of an adsorbate:

$$G = E + ZPE - TS \quad (2)$$

where ZPE is the zero-point energy, E represents the total energy, T is the temperature in Kelvin (in this case, set as 333.15 K), and S represents the entropy.

3. Result and discussion

3.1. Characterization of Ca-doped Cu-based catalysts

To obtain the surface and pore properties of samples, the N₂ adsorption-desorption experiment was performed (Fig. 1 and Table 1). The prepared catalysts were designated as Cat_{CaxCu3}, where x represents the mass fraction (%) of calcium, and the mass fraction (%) of copper defaults to 3±0.1%. As shown in Fig. 1, all the isotherms of the samples exhibited a type IV shape with a distinct H3 hysteresis loop. Such hysteresis loops are typically observed in materials with slit-shaped pores that have non-uniform size and/or shape [36]. Table 2

The pore widths of all samples are in the range of 3–11 nm, indicating that they all possess a typical mesoporous structure [37]. It can be observed that with the increase in metal content, the H3 hysteresis loop shifts towards higher P/P₀ values, indicating a narrower distribution range of pores. This suggests that the metal may preferentially occupy smaller pores during loading. The Ca/Al₂O₃ sample has the largest SSA, with 2–3 nm smaller pore sizes than those of the Al₂O₃ matrix, while the pores in other width ranges remain almost constant. The total pore volume (TPV) did not decrease, but the average pore width was reduced. This may be attributed to the growth of microporous nanosheets on the surface of the Ca/Al₂O₃ sample. The SSA of the Cat_{Cu3} decreased with the loading of Cu oxides, and further decreased with the loading of Ca-compounds due to the deposition of metal oxides in minute pores (2–3 nm). It can be found that the SSA of Cat_{Ca2.5Cu3} exhibits a significant increase, which may be attributed to the formation of microporous nanosheets. However, the low SSA of Cat_{Ca3Cu3} suggests that the formation of nanosheets requires a specific concentration. Furthermore, the largest TPV and pore width of Cat_{Ca2.5Cu3} suggested that the nanosheets composed of CuO and Ca-compounds have more micropores and mesopores than those grown by Ca-compounds. This implies that there are more H₂S adsorption and conversion sites and additional product storage space available, which is advantageous for H₂S removal [38,39].

The related samples were studied by SEM to gain insights into the influence of Ca compounds on the morphology of catalysts. Representative micrographs of all samples are shown in Fig. S5. For comparison, images of Al₂O₃ are also presented. A three-dimensional (3D) nano-sheet structure can be observed on the surface of Ca/Al₂O₃, which is the reason for its high SSA. In contrast, the Cu/Al₂O₃ surface exhibits rough and uneven particles, but after adding Ca, irregular small particles of various sizes appear on the catalyst surface. As the content of Ca-compounds on the surface increases, these particles gradually accumulate. When the Ca content reaches 2.5 wt%, the catalyst displays a layered structure with nano-sheets (Fig. S6). However, with further increases in Ca compound content, these particles gradually agglomerate into larger clusters and the nano-sheet structure disappears. The SEM morphology change of the catalyst explains the reason for the increase and then decrease in SSA with increasing Ca content. Additionally, the

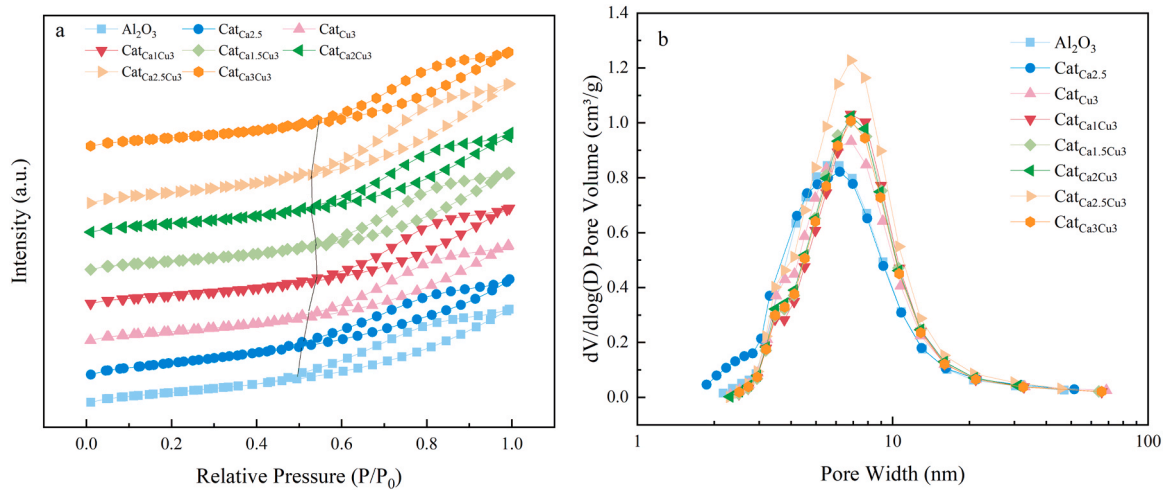


Fig. 1. The N_2 adsorption-desorption isotherms (a) and pore width (b) of $Cat_{Ca/Cu}$.

Table 1
The properties of all $Cat_{Ca/Cu}$.

Sample	Metal content (wt%)		SSA (m^2/g)	TPV (cm^3/g)	Average Pore width (nm)
	Ca	Cu			
Al_2O_3	0	0	231	0.45	6.1
$CaO/Ca(NO_3)_2$	/	/	18	0.03	/
CuO	/	/	15	0.04	/
$Cat_{Ca2.5}$	2.5	0	267	0.45	5.8
Cat_{Cu3}	0	3	204	0.45	6.6
Cat_{Ca1Cu3}	1	3	196	0.45	6.9
$Cat_{Ca1.5Cu3}$	1.5	3	191	0.45	7.0
Cat_{Ca2Cu3}	2	3	198	0.44	6.7
$Cat_{Ca2.5Cu3}$	2.5	3	245	0.56	6.8
Cat_{Ca3Cu3}	3	3	193	0.44	6.8
$Cat_{Ca2.5Cu3-S}$	2.5	3	64	0.22	7.6

Table 2
Peak areas of different basic sites in CO_2 -TPD.

Catalyst	Basicity site				Total
	weak	medium	strongly	Medium and strongly	
Cat_{Cu3}	0.060	0.065	0.063	0.128	0.187
$Cat_{Ca2.5}$	0.117	0.197	0.181	0.378	0.495
Cat_{Ca1Cu3}	0.075	0.078	0.068	0.146	0.221
$Cat_{Ca1.5Cu3}$	0.067	0.104	0.079	0.183	0.250
Cat_{Ca2Cu3}	0.068	0.100	0.094	0.195	0.262
$Cat_{Ca2.5Cu3}$	0.080	0.107	0.180	0.286	0.366
Cat_{Ca3Cu3}	0.071	0.111	0.110	0.221	0.292

EDX image shows that Cu and Ca are highly and uniformly dispersed throughout the catalyst.

To verify the influence of supported metal on the crystalline structure of samples, XRD patterns were measured (Fig. 2a). The result showed that all samples presented a crystal phase of $\gamma-Al_2O_3$, and no peaks belonging to Cu oxides and Ca-compounds were discovered, indicating the high dispersion of metals.

To further investigate the active composition of $Cat_{Ca/Cu}$, XPS analysis was implemented (Fig. 2). The spin-orbit splitting separation δ ($Ca\ 2p_{3/2} - Ca\ 2p_{1/2}$) of Ca-compound is $3.5 \pm 0.2\ eV$ [40]. As shown in Fig. 2b, the $Ca\ 2p$ of $Cat_{Ca2.5}$ was deconvoluted into four different characteristic peaks, whereas in $Cat_{Ca2.5Cu3}$, there are only two deconvoluted distinct peaks. Among them, the characteristic peaks at ca. 346.4 eV and ca. 359.8 eV correspond to $2p_{3/2}$ and $2p_{1/2}$ peak of CaO respectively [40,

41], while the characteristic peak at ca. 348 eV and ca. 351.5 eV were corresponding to $2p_{3/2}$ and $2p_{1/2}$ characteristic peak of $CaCO_3$ or $Ca(NO_3)_2$ which was not completely pyrolyzed [40]. To further verify the presence of Ca-compounds, the $C\ 1s$ diffraction patterns $Cat_{Ca2.5}$ and Cat_{Cu3} were compared (Fig. 2c), and it can be observed that no other characteristic peak was present except for the C-C peak (284.8 eV) and C=O peak (289 eV) caused by carbon pollution [42]. As a result, the characteristic peak of the $Ca\ 2p$ diffraction pattern at ca. 348 eV was not corresponding to $CaCO_3$ [43,44]. To further demonstrate the existence form of Ca, thermogravimetric (TG) and differential thermogravimetric (DTG) analyses were performed on $Ca(NO_3)_2 \cdot 4H_2O$ within the calcination range of 30–800 °C.

As shown in Fig. 2g, the weight loss of the $Ca(NO_3)_2 \cdot 4H_2O$ in the N_2 atmosphere started at 30 °C, a slow mass loss of 4.6% occurred between 30 °C and 129.45 °C, followed by a rapid mass loss of 24.81% until 235.8 °C. According to the DTG results, $Ca(NO_3)_2 \cdot 4H_2O$ experienced three weight loss stages below 800 °C: The first stage involves the removal of adsorbed water and crystalline water. In contrast, the second stage involves the removal of crystalline water, and the third stage involves the release of O_2 and NO . The total weight loss below 500 °C is 29.41%, which is similar to the weight loss of $Ca(NO_3)_2 \cdot 4H_2O$ when completely dehydrated into $Ca(NO_3)_2$. Although $Ca(NO_3)_2$ may undergo further decomposition at 490 °C, the presence of $\gamma-Al_2O_3$ promotes this process, while the presence of Cu_xO slows it down [45]. Based on XPS results, the surface of $Cat_{Ca2.5}$ contains both $Ca(NO_3)_2$ and CaO , whereas the surface of $Cat_{Ca2.5Cu3}$ only contains $Ca(NO_3)_2$.

The $O\ 1s$ peaks of $Cat_{Ca/Cu}$ samples were further analyzed in Fig. 2d, the peaks located at ca. 530.1 eV (O-I), ca. 531 eV (O-II), ca. 532 eV (O-III) and ca. 532.8 eV (O-IV) are assigned to the lattice oxygen in CuO [46] or/and CaO [47], chemisorbed oxygen, lattice oxygen in Al_2O_3 [48], and hydroxyl oxygen and/or surface adsorbed oxygen. In the $Cat_{Ca/Cu}$ samples, the O-III content corresponds to the VOs concentration [48–50]. The O-IV of Cat_{Cu3} was attributed to the oxygen species that are weakly bound (such as H_2O or O_2 adsorbed onto the catalyst's surface) and/or -OH groups, for $Cat_{Ca2.5Cu3}$ and $Cat_{Ca2.5}$, the O-IV might also be related to O in NO_3 . The surface of the $Cat_{Ca2.5}$ catalyst showed the presence of only three oxygen species, but no O-II was detected, suggesting that there were no VOs on the surface of $Cat_{Ca2.5}$. The percentage of O-II for Cat_{Cu3} and $Cat_{Ca2.5Cu3}$ are 31.89% and 40.9%, respectively. The higher proportion of VOs in $Cat_{Ca2.5Cu3}$ indicates stronger surface reactivity, leading to improved interactions with H_2S during the removal process [51].

Fig. 2e shows the characteristic peaks of $Cu\ 2p_{3/2}$ of Cat_{Cu3} and $Cat_{Ca2.5Cu3}$, deconvoluted into two peaks. The binding energy characteristic peak at ca. 934.7 eV implies the existence of $Cu(II)$, and the peak

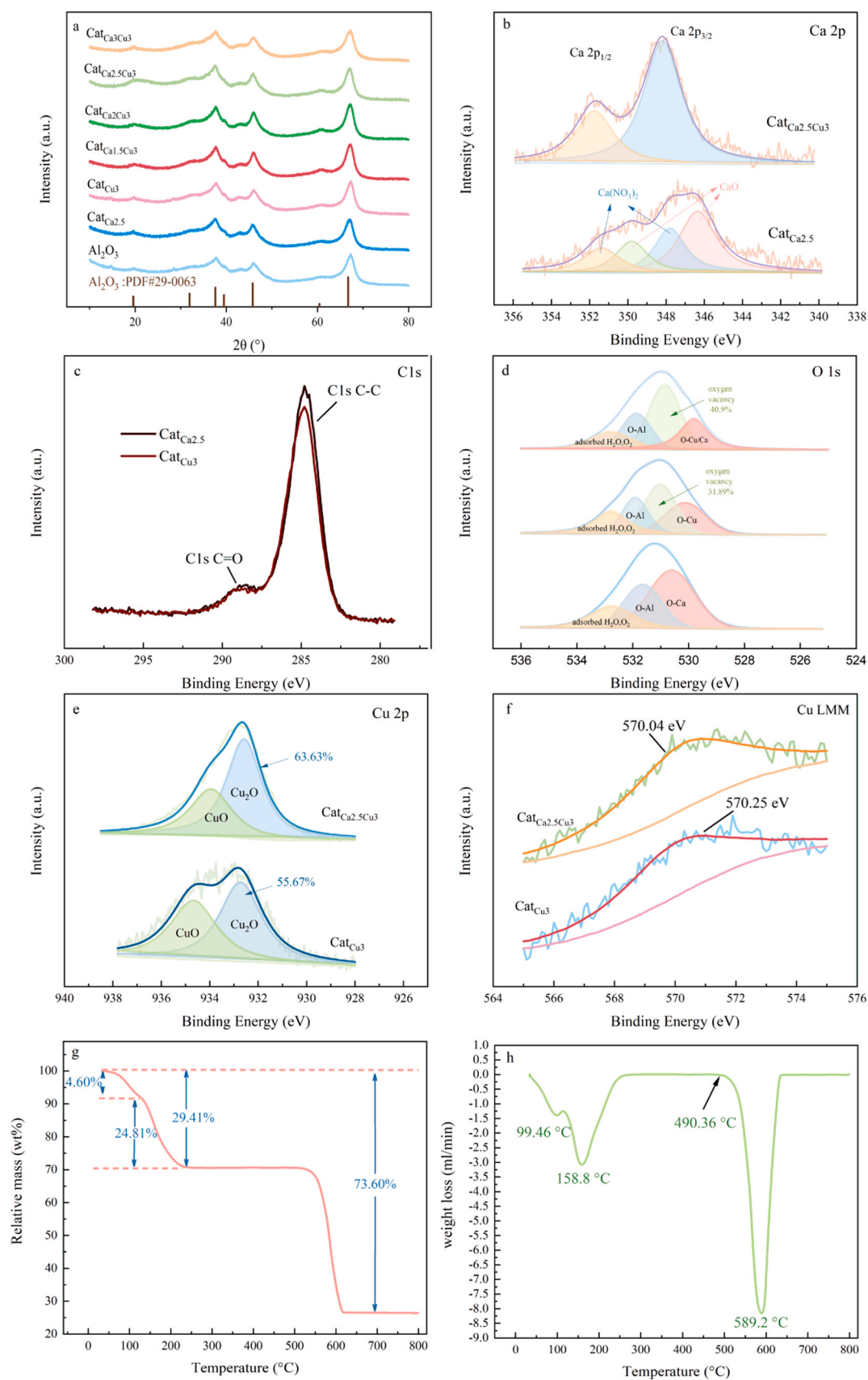


Fig. 2. XRD (a), XPS of Ca 2p (b), C 1s (c), O 1s (d), Cu 2p (e), and Cu LMM (f) pattern of $\text{Cat}_{\text{Ca}_x\text{Cu}_3}$, and TG (g) and DTG (h) of $\text{Cat}_{\text{Ca}_2.5\text{Cu}_3}$.

at ca. 932.8 eV corresponds to the Cu(0)/Cu(I) [52,53]. To identify the existence of Cu(0) and Cu(I), Cu LMM peaks can be used to distinguish these copper species. As shown in Fig. 2f, the Cu LMM peaks of Cat_{Cu3} and Cat_{Ca2.5Cu3} occurred at ca. 570 eV, indicating the existence of Cu(I) [54,55]. The change of binding energy of Cu 2p and Cu LMM after introducing Ca-compounds suggests the presence of a chemical bonding interface between Cu oxides and Ca-compounds rather than just physical contact between two separate phases [56]. Moreover, the introduction of Ca(NO₃)₂ increases the proportion of Cu(I) peak area (from 55.67% to 63.63%), which may be attributed to the doping of Ca(NO₃)₂·4 H₂O. As a result, some of the Cu(II) species gain electrons and transform into Cu(I) [57,58]. The formation of partial VOs is achieved by eliminating some O atoms from the CuO [59].

To investigate the fine structure of Cat_{Ca2.5Cu3} nano-sheets further, the TEM images and crystal size distribution (Fig. 3) were also analyzed. As a comparison, TEM of Al₂O₃ is also provided in Fig. S7. Plentiful nanoparticles and their crisscross needle-like structures can be observed in the TEM image of Cat_{Ca2.5Cu3} (Fig. 3a). From Fig. S7, the overall thickness of Al₂O₃ is greater than Cat_{Ca2.5Cu3}, with Al₂O₃ featuring overlapping edge sheets, while the edges of Cat_{Ca2.5Cu3} are evidently extended into thin nanosheets. This result is consistent with the SEM results, confirming the formation of nanosheets on the surface of Ca_{2.5}Cu₃. Also, numerous uniformly distributed pores with sizes less than 1 nm on the nanosheets (indicated by the red circles in Fig. 3c). The enlarged HRTEM image (Fig. 3c) shows obvious lattice fringes, the

lattice fringes of 0.232, 0.216, 0.150 and 0.257 nm were attributed to the (111) lattice plane of CuO, the (006) lattice plane of Al₂O₃, the (220) lattice plane of Cu₂O, and the (001) lattice plane of Ca(NO₃)₂, respectively. Furthermore, the HRTEM images were subjected to fast Fourier transform (FFT) and inverse FFT analysis (Fig. S8). The results indicated that the nanosheets were formed by the staggered combination of metals with different crystal structures. Still, the composition of each part was different, which indicated that CuO, Cu₂O, and Ca(NO₃)₂ coexisted in the nanosheets, whereas the distribution was random. In addition, Fig. 3b showcases a selected area electron diffraction (SAED) image of a portion of the nanosheet. This image indicated that the Cat_{Ca2.5Cu3} exhibited polycrystalline characteristics, and the concentric diffraction ring pattern can be assigned to the CuO (111), Al₂O₃ (006), and Ca(NO₃)₂ (001), respectively.

To further verify the existence of VOs, EPR measurements were performed. For Cu-based catalysts, the EPR spectrum (Fig. 4a) shows visible EPR signals, and after adding the Ca compounds, the vacancy signal increased. The Cat_{Ca2.5Cu3} exhibited the highest EPR signal, and the signal at 60 °C was higher than that at 25 °C (Fig. 4b), which showed that slight heating was beneficial to the activation of more VOs. In contrast, there was no appreciable signal of Ca/Al₂O₃, suggesting that no VOs existed in Ca/Al₂O₃, and VOs were primarily formed due to the oxygen deficiency in Cu_xO. The doping of Ca-compounds resulted in the shedding of oxygen from the Cu_xO lattice (the proportion of Cu(I) increased) resulting in the formation of more VOs, which was consistent

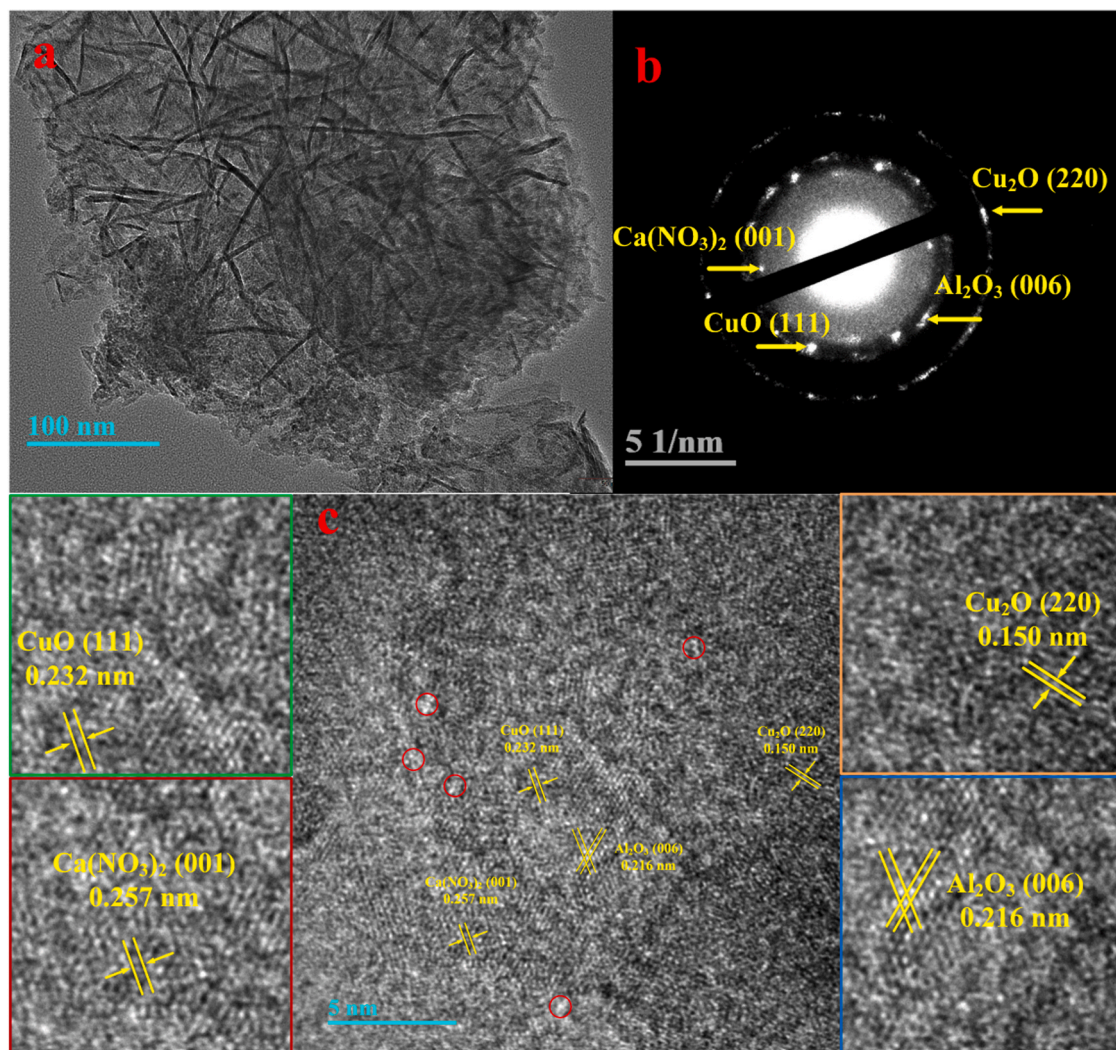


Fig. 3. TEM (a), SAED (b), and HRTEM (c) image of Cat_{Ca2.5Cu3} nanosheet.

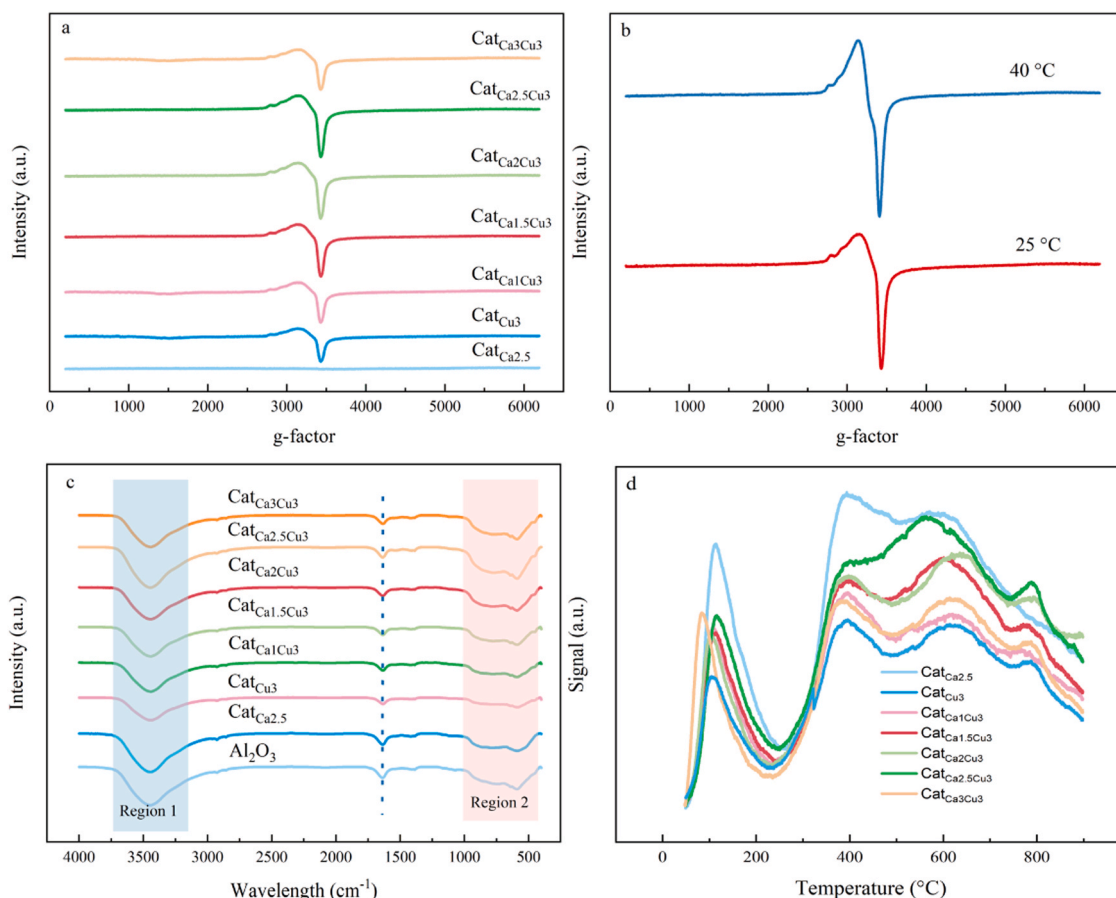


Fig. 4. EPR-vacancy of all Ca-Cu/Al₂O₃ catalysts (a), and Cat_{Ca2.5}Cu₃ at different temperatures (b), CO₂-TPD (c) and FTIR (d) of all Ca-Cu/Al₂O₃ catalysts.

with the XPS results.

Results from FT-IR measurements were depicted in Fig. 4c, and the spectra of Al₂O₃ were presented for reference purposes. The peaks attributed to -OH stretching were identified in region 1 (3300–3600 cm⁻¹), while the vibrations related to M²⁺-O²⁻ were shown in the peaks <1000 cm⁻¹ (region 2). The peak at 1630 cm⁻¹ corresponded to O-CO stretching or H-OH bending vibrations [3,23]. To gain insight into the distribution of basic sites on the catalyst surface, CO₂-TPD analysis was performed. Basic sites were classified into weak (<300 °C), medium (300–500 °C), and strong (>500 °C) based on CO₂ desorption temperature (Fig. 4d, Fig. S9) [60]. The CO₂ peak below 300 °C represented CO₂ desorption adsorbed on the catalyst surface hydroxyl groups, while the peak at 300–500 °C was related to M²⁺-O²⁻ acid-base pairs [60]. According to FTIR results, hydroxyl groups were related to the hydrophilicity of Al₂O₃, which was beneficial to removing H₂S. In general, peaks above 500 °C indicated coordination of unsaturated O²⁻, with higher concentrations indicating more VOs on the catalyst. EPR-vacancy results showed no VOs in Cat_{Ca2.5}, but the Cat_{Ca2.5} exhibited the strongest CO₂ desorption peak in the range of 500–700 °C, indicating that this peak was not related to VOs. The Cu-based catalyst showed four CO₂ adsorption characteristic peaks. In contrast, the Ca/Al₂O₃ sample had only three surface basic sites, indicating that the peaks around 800 °C were ascribed to the coordination of unsaturated O²⁻. The 500–700 °C peaks may be attributed to the interaction between the highly dispersed Ca(NO₃)₂/Cu_xO and the Al₂O₃ support [61]. The presence of this complex strong basic site may enhance the desulfurization effect of the Cu-based catalyst. Correlational analysis between sulfur capacity and areas of three different basic sites and total basic site area (Fig. S10) indicated a strong correlation between sulfur capacity and total basic site area ($R^2 = 0.87$), with a higher correlation between

sulfur capacity and medium strong basic sites than weak basic sites. These findings suggested that catalyst surface basic sites positively correlate with desulfurization performance, with surface metal basicity and VOs working synergistically to promote desulfurization.

Basic sites generally exhibit the capability to adsorb and concentrate free radicals [62,63]. This implies that the basic sites might adsorb the ·OH produced by the catalysis of VOs in H₂O. EPR spectroscopy (Fig. 5) was employed to test this hypothesis to investigate the unpaired electron spins in the catalysts, revealing valuable structural information [64].

The results showed that no signal attributed to unpaired electron states was observed in the EPR spectrum of Cat_{Ca2.5} without VOs, indicating that this catalyst does not possess the ability to generate ·OH. For Cu-based catalysts, the presence of ·OH was observed to be consistent with the trend of VOs but not directly proportional. All Cu-based catalysts exhibited a significant amount of ·OH, indicating that the doping of Ca(NO₃)₂ increased the VOs in the catalysts, provided basic sites, and enabled the enrichment of ·OH. This adsorptive and enrichment effect plays a crucial role in stabilizing free radicals and creates additional opportunities for subsequent catalytic reactions. Moreover, EPR tests were conducted under different time (Fig. 5b) and temperature (Fig. 5c) conditions, revealing that the catalyst acquires ·OH through its catalytic action on the DMPPO, with higher temperatures enhancing this process.

3.2. Catalytic performance

Different Cu-based catalysts with varying Ca metal content were subjected to dynamic H₂S oxidation adsorption experiments (Fig. 6a, b). The results show that the alumina support had no removal performance on H₂S, while Ca/Al₂O₃ had very little performance, with a breakthrough sulfur capacity of approximately 12.86 mg H₂S/g catalyst. Cu/

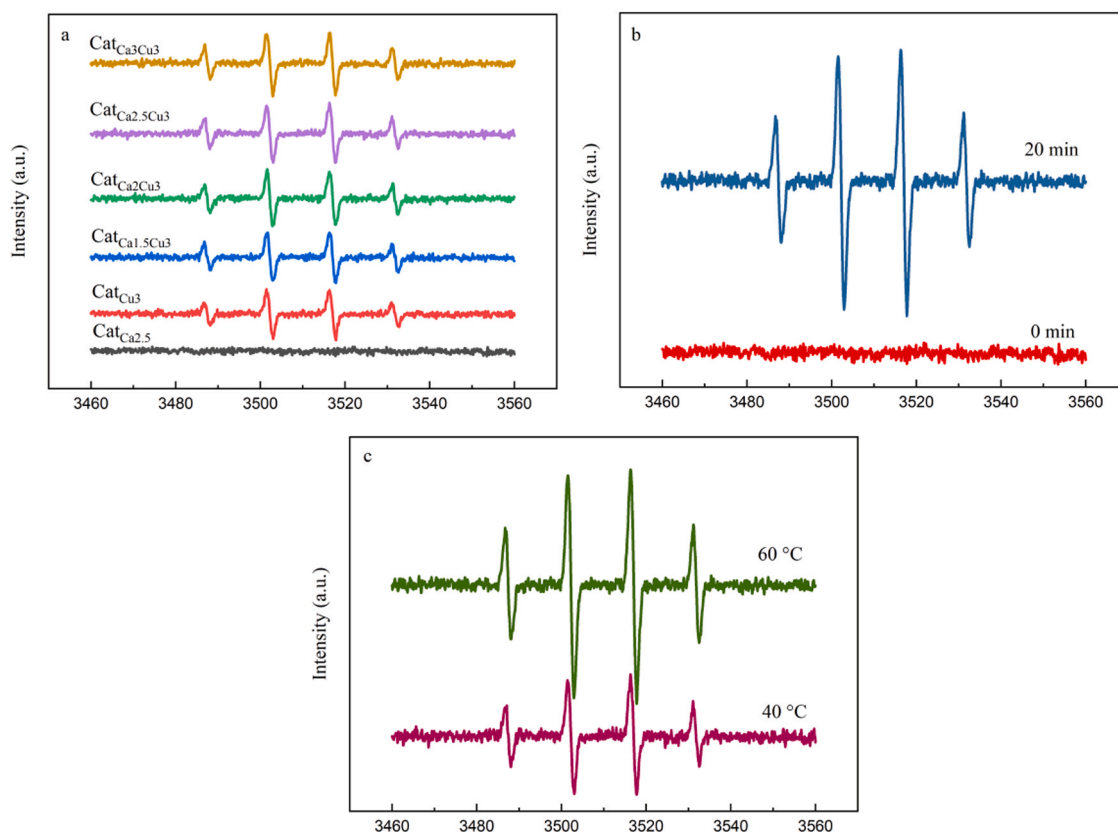


Fig. 5. EPR spectra of $\text{Cat}_{\text{Ca}x\text{Cu}3}$ catalysts (a), $\text{Cat}_{\text{Ni}2.5\text{Cu}3}$ at different time points (b) and different temperature (c).

Al_2O_3 had an ideal catalytic oxidation effect on H_2S , with a breakthrough sulfur capacity of up to 225.27 mg/g, increasing the breakthrough sulfur capacity with increasing Ca content. The maximum sulfur capacity was observed at a Ca content of 2.5 wt%, reaching 401.34 mg/g.

The catalytic mechanism of the catalyst can be understood by examining its theoretical sulfur capacity (TSC) (Eq. 3). Additionally, The SSA sulfur capacity and the TPV sulfur capacity are also included in the analysis (Table 3).

$$\text{TSC} = \frac{m}{M_{\text{metal}}} \times M_{\text{H}_2\text{S}} \times 1000 \quad (3)$$

Where: TSC is the theoretical sulfur capacity of the catalyst (mg H_2S /g catalyst), M_{metal} is the atomic mass of a metal substance (g/mol), m is the metal's mass per catalyst (1 g), $M_{\text{H}_2\text{S}}$ is the molecule mass of H_2S (34 g/mol)

Al_2O_3 , Cu_xO , and Ca-compounds among the prepared catalysts exhibited significantly low H_2S desulfurization capacity. However, both Cu_xO and Ca-compounds demonstrated the highest surface activity, suggesting that the primary active components were Cu_xO and Ca (NO_3)₂. The sulfur capacity of $\text{Cat}_{\text{Ca}2.5}$ was lower than the TSC, indicating that Ca/ Al_2O_3 only underwent chemical adsorption and lacked catalytic oxidation of H_2S . The sulfur capacities of all Cu-based catalysts were higher than the TSC, indicating that there was also catalytic oxidation of H_2S in addition to chemical adsorption. While individual Ca-compounds did not exhibit catalytic oxidation performance on H_2S , adding it to Cu/ Al_2O_3 can promote the catalytic activity of Cu-based catalysts. Furthermore, although $\text{Cat}_{\text{Ca}2.5\text{Cu}3}$ had the highest sulfur capacity, the SASC and TVSC were lower than those of other Cu-based catalysts. This indicated that for $\text{Cat}_{\text{Ca}x\text{Cu}3}$, the SSA and pore volume are not the limiting factors for desulfurization. The larger SSA increased the exposure of active sites, thus enhancing the catalyst's performance. However, during the reaction, the generation of desulfurization by-

products led to the collapse of the catalyst's surface nano-sheet structure, gradually diminishing the catalytic reaction. Consequently, the full utilization of the SSA and pore volume could not be achieved.

To evaluate the influence of H_2O on the removal of H_2S , dynamic H_2S removal experiments were performed at different levels of humidity (Fig. 6e, f) and the figure depicting the state of the samples before and after the reaction under different humidity conditions was presented in Fig. S11 and Fig. S12. The results demonstrated the significant influence of H_2O on the catalytic removal of H_2S . In the absence of H_2O , the breakthrough sulfur capacity of H_2S was only 33.6 mg/g, which is below the TSC. However, under RH 40% and 60%, the catalyst surpassed the TSC by a considerable margin, implying that the catalytic reaction can only persist in the presence of H_2O . Moreover, investigators observed that water vapor also enhances the elimination of H_2S by facilitating the dissociation of captured H_2S . Additionally, at a relative humidity of 80%, excessive moisture caused catalyst agglomeration (Fig. S12c), preventing H_2S from reaching the catalyst's active sites and impeding the reaction. Hence, maintaining a suitable level of H_2O content is critical to ensure effective catalytic oxidative removal of H_2S .

Dynamic removal experiments of H_2S with $\text{Cat}_{\text{Ca}2.5\text{Cu}3}$ were conducted at various room temperatures (Fig. 6e, f), and the results indicated that the temperature had a certain impact on H_2S elimination. The desulfurization performance of the catalyst was enhanced within 40–60 °C, whereas further increasing the temperature led to a decrease. This may be attributed to the positive role that an appropriate temperature played in promoting the diffusion of H_2S to the surface of the catalyst, fostering the catalytic reaction. In contrast, excessively high temperatures hindered the physical adsorption of H_2S and H_2O on the surface of the catalyst.

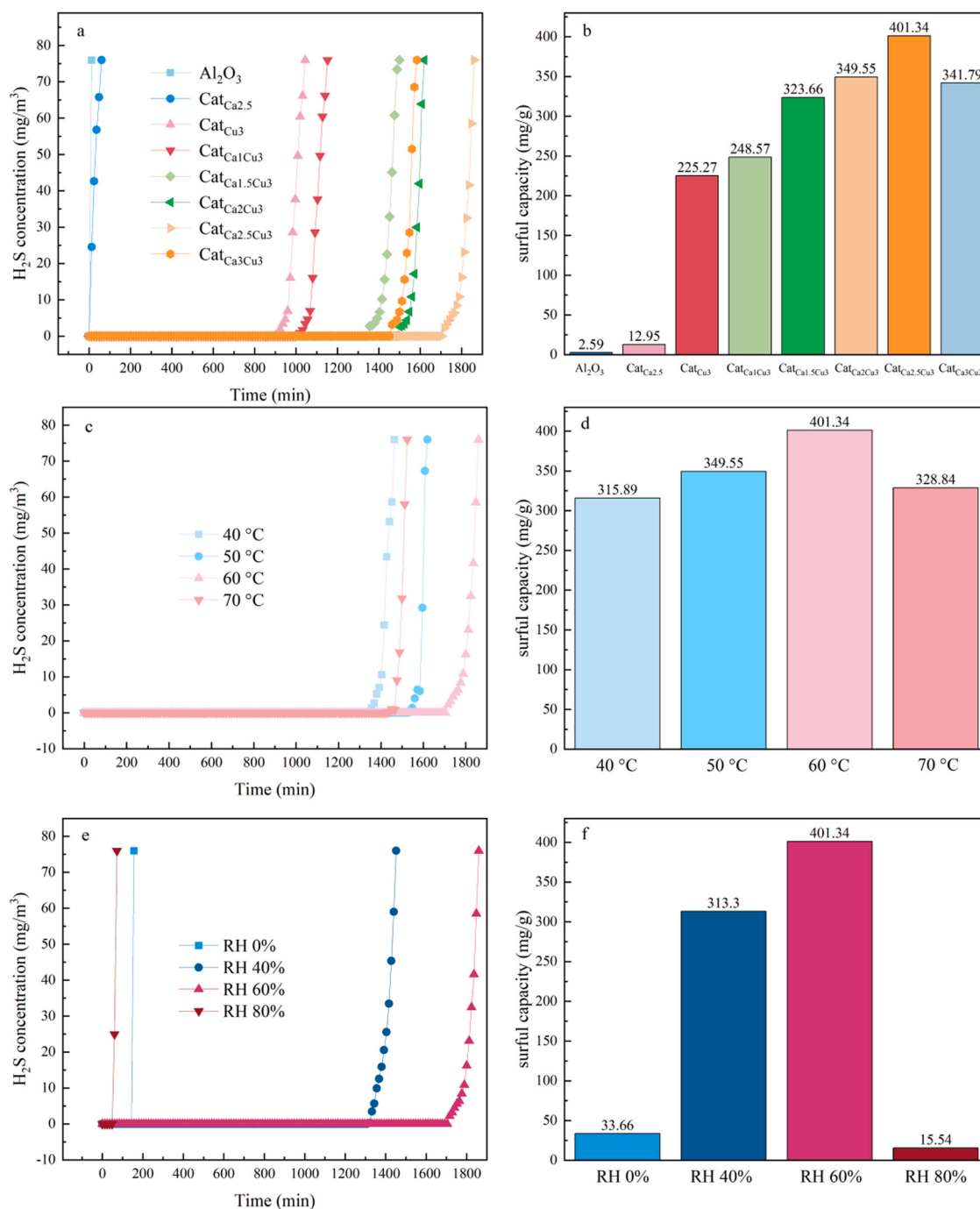


Fig. 6. Breakthrough curves and breakthrough sulfur capacity for catalytic oxidation of H_2S of $\text{Cat}_{\text{Ca}x\text{Cu}3}$ at 60 °C and relative humidity 60% (a, b) and breakthrough curves and breakthrough sulfur capacity of $\text{Cat}_{\text{Ca}2.5\text{Cu}3}$ at different humidities (c, d) and relative temperatures (e, f).

3.3. Mechanisms of $\text{Cat}_{\text{Ca}2.5\text{Cu}3}$ desulfurization

3.3.1. Analysis of spent catalysts

Fig. S13 displays the N_2 adsorption-desorption and SEM results of the $\text{Cat}_{\text{Ca}2.5\text{Cu}3}$ catalyst before and after H_2S desulfurization. The overall structure of the catalyst remained unaffected by the desulfurization process, which still maintained the mesoporous structure with H_3 -type hysteresis loop (Fig. S13a). However, the hysteresis loop weakened. According to the pore size distribution, the reactive adsorption of H_2S resulted in a reduction of the pore capacity of the catalyst (Fig. S13b, Table 1), indicating that desulfurization products were stored in the pore structure. The SEM results (Fig. S13d) showed that the agglomerates

generated during catalyst desulfurization covered the surface and the layered structure and nanosheets disappeared. According to EDS results (Fig. S13e), elemental sulfur and sulfur compounds covered the catalyst's surface while Cu and Ca compounds were hardly detectable.

To identify the H_2S desulfurization product on the catalyst, we conducted XRD and XPS analyses on the spent catalysts. XRD pattern of $\text{Cat}_{\text{Ca}2.5\text{Cu}3}\text{-S}$ (Fig. 7a) proved that the H_2S desulfurization product adsorbed in the deep pore structure was mainly sulfur (PDF#99-0066), and no sulfate or sulfide with Ca or Cu were detected, which may be related to the content lower than the XRD detection limit or high degree of metal dispersion.

The XPS analysis was conducted to further identify the

Table 3

Theoretical sulfur capacity and actual sulfur capacity of samples.

Samples	TSC (mg/g)	Sulfur capacity		
		mg/g	mg/m ²	mg/m ³
Al ₂ O ₃	/	2.59	0.01	5.76
CaO/Ca(NO ₃) ₂	Ca. 300	10.9	0.61	363.33
Cu _x O	531.2	18	1.20	450.00
Cat _{Ca2.5}	21.25	12.95	0.05	28.78
Cat _{Cu3}	16.5	225.27	1.10	500.60
Cat _{Ca1Cu3}	24.43	248.57	1.27	552.38
Cat _{Ca1.5Cu3}	28.68	323.66	1.69	719.24
Cat _{Ca2Cu3}	32.93	349.55	1.77	794.43
Cat _{Ca2.5Cu3}	37.18	401.34	1.64	716.68
Cat _{Ca3Cu3}	41.43	341.79	1.77	776.80

desulfurization product on the surface of the catalysts. Fig. 7b shows the S 2p region of the three samples, in this region, the spectrum of Cat_{Cu3} and Cat_{Ca2.5Cu3} was deconvoluted into 6 peaks. The BEs of S 2p_{3/2} and S 2p_{1/2} appeared at ca. 161.7 eV and 162.8 eV, respectively, suggesting the presence of S in S²⁻ [65–67]. The BEs at ca. 163.7 eV and ca. 164.7 eV corresponded to the 2p_{3/2} and S 2p_{1/2} of elemental S. Moreover, the peaks appear at ca. 168.6 eV and ca. 169.8 eV correspond to the 2p_{3/2} and 2p_{1/2} characteristic peak of SO₄²⁻ [68], indicating the further oxidation of elemental S. It was worth noting that Cat_{Ca2.5Cu3} has 0.1 eV shift compared with Cat_{Cu3}, which may be due to the existence of S compounds related to Ca. For Cat_{Ca2.5}, although a weak S 2p characteristic peak could be detected, it could not be deconvoluted clearly, and thus the desulfurization product will be judged by Ca 2p. The surface total sulfur content detected by XPS in Cat_{Ca2.5}, Cat_{Cu3}, and Cat_{Ca2.5Cu3} was 2.44%, 16.19%, and 23.89%, respectively. The sulfate detected on the surface was the dominant product for Cat_{Cu3} and Cat_{Ca2.5Cu3}, accounting for 59.85% and 64.8% respectively, indicating that the doping of Ca(NO₃)₂ not only increased the desulfurization performance, but also promoted the conversion of desulfurization products to sulfate.

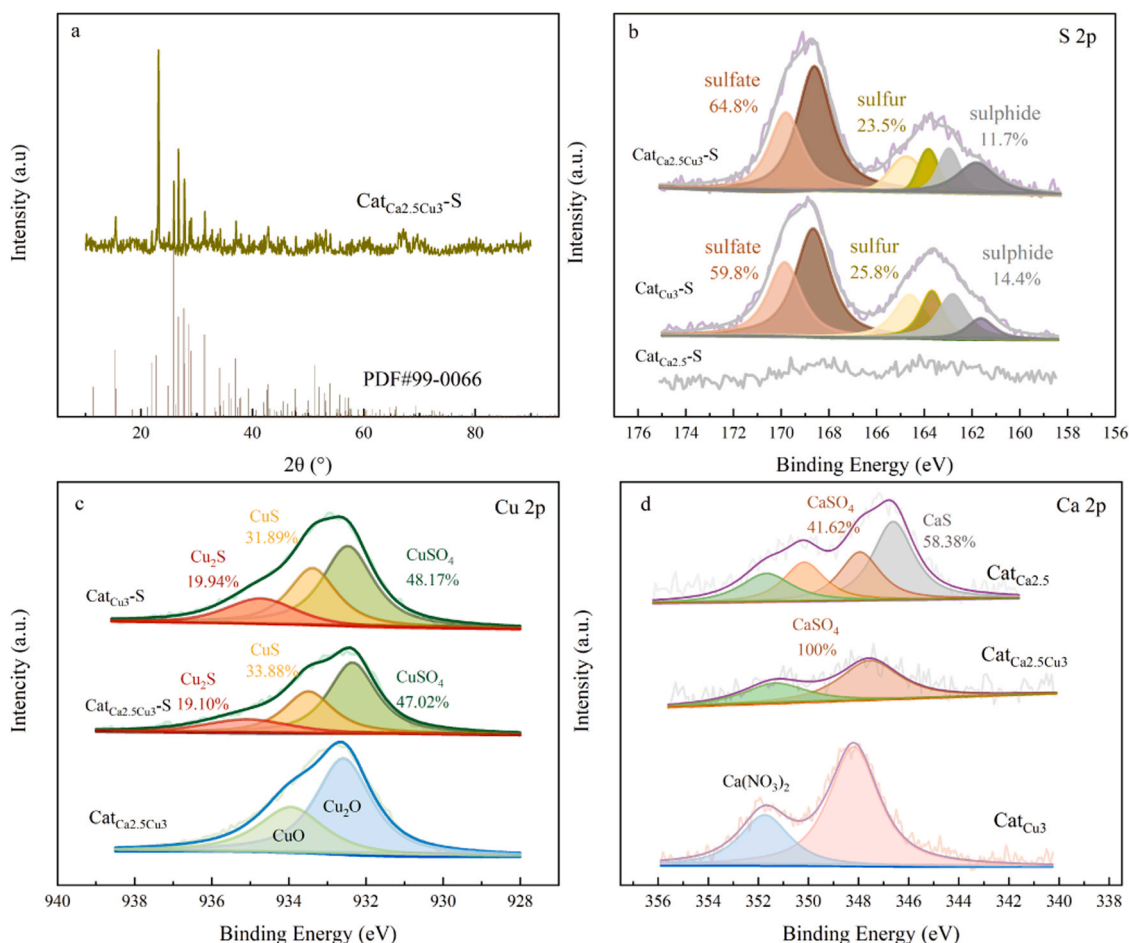
The Cu 2p_{3/2} peaks of Cat_{Cu3} and Cat_{Ca2.5Cu3} (Fig. 7c) were deconvoluted into three distinct peaks at ca. 934.9 eV, ca. 933.3 eV, and ca. 932.2 eV, corresponding to the presence of CuSO₄, Cu₂S, and CuS, respectively [69–72]. Furthermore, the Ca 2p peaks of Cat_{Ca2.5} (Fig. 7d) can be deconvoluted into 4 distinct characteristic peaks. Among them, the characteristic peaks at ca. 346.5 eV and ca. 350.1 eV correspond to 2p_{3/2} and 2p_{1/2} of CaS respectively [73], while the characteristic peak at ca. 347.8 eV and ca. 351.4 eV were corresponding to 2p_{3/2} and 2p_{1/2} characteristic peak of CaSO₄ [74]. It is worth noting that the Cat_{Ca2.5Cu3} only exhibits characteristic peaks corresponding to CaSO₄, and combined with the S 2p results, it can be concluded that the doping of Ca(NO₃)₂ promotes the oxidation of S.

The detected sulfur content of the Cat_{Ca2.5} was 2.44%, which is almost identical to the loaded Ca content. This suggested that the desulfurization process of Cat_{Ca2.5} did not generate elemental sulfur. As a result, according to XPS analysis, when only loaded with Ca, the desulfurization products of the catalyst consist of sulfides and sulfates. However, for Cat_{Cu3} and Cat_{Ca2.5Cu3}, the desulfurization process yields sulfides, sulfates, and sulfur. In conclusion, the desulfurization products of Cat_{Ca2.5Cu3} include CaSO₄, CuSO₄, CuS, and S.

The detected sulfur content of the Cat_{Ca2.5} was 2.44%, which is almost identical to the loaded Ca content. This suggested that the desulfurization process of Cat_{Ca2.5} did not generate elemental sulfur. As a result, according to XPS analysis, when only loaded with Ca, the desulfurization products of the catalyst consist of sulfides and sulfates. However, for Cat_{Cu3} and Cat_{Ca2.5Cu3}, the desulfurization process yields sulfides, sulfates, and sulfur. In conclusion, the desulfurization products of Cat_{Ca2.5Cu3} include CaSO₄, CuSO₄, CuS, and S.

3.3.2. DFT calculations

The dynamic H₂S removal experimental results demonstrate the crucial role of H₂O in the catalytic removal of H₂S. However, Ca/Al₂O₃

**Fig. 7.** The XRD (a) and XPS, S 2p (b), Cu 2p (c), and Ca 2p (d) image of Cat_{Ca_xCu₃}.

catalysts without VO did not exhibit catalytic H₂S activity, whereas Cu-based catalysts with VOs exhibited efficient desulfurization. This indicates that Cu-based catalysts achieve catalytic oxidation of H₂S at low temperatures by leveraging the catalytic action of VOs species on H₂O. DFT calculations were used to investigate the impact of Ca(NO₃)₂-doping on the formation of VOs. The formation energy of VOs (eV) was determined using the formula: $E_V = E_{\text{tot(def)}} - E_{\text{tot(no def)}} + \frac{1}{2}E_{O_2}$. Here, $E_{\text{tot(def)}}$ and $E_{\text{tot(no def)}}$ represent the energy of defective systems or perfect surface, E_{O_2} means the energy of an O₂ molecule. The formation energies of VOs for these two structures were calculated to be -0.75 eV and -1.336 eV, respectively. These results indicate that the formation of VOs in both catalysts is spontaneous, and the presence of Ca(NO₃)₂ facilitates the formation of VOs. This observation aligns with the trend observed in the EPR-defect results.

The reaction pathway of critical steps was calculated using the transition state (TS) theory. Fig. 8a, b presented the calculations of the adsorption of H₂O and its catalytic behavior on the VOs. The computational results showed that for the Cu_xO/Al₂O₃ catalyst, the adsorption of H₂O and its catalytic conversion to OH at the Cu₂O site is spontaneous (-0.37 eV) (Fig. 8a). The VOs in Cu₂O catalyze the hydroxylation of H₂O (Eq. 4) without undergoing chemical reaction (Eq. 5). And it becomes even more favorable with the doping of Ca(NO₃)₂ (-1.21 eV). Although the hydroxylation of H₂O at the CuO site is also spontaneous (Fig. 8b), the formation of the transition state (Cu(OH)₂) requires some energy. However, this reaction becomes more favorable after doping Ca(NO₃)₂. Combining experimental and characterization results, it can be concluded that the basis for the H₂S-catalyzed oxidation is the hydroxylation of H₂O by VOs.

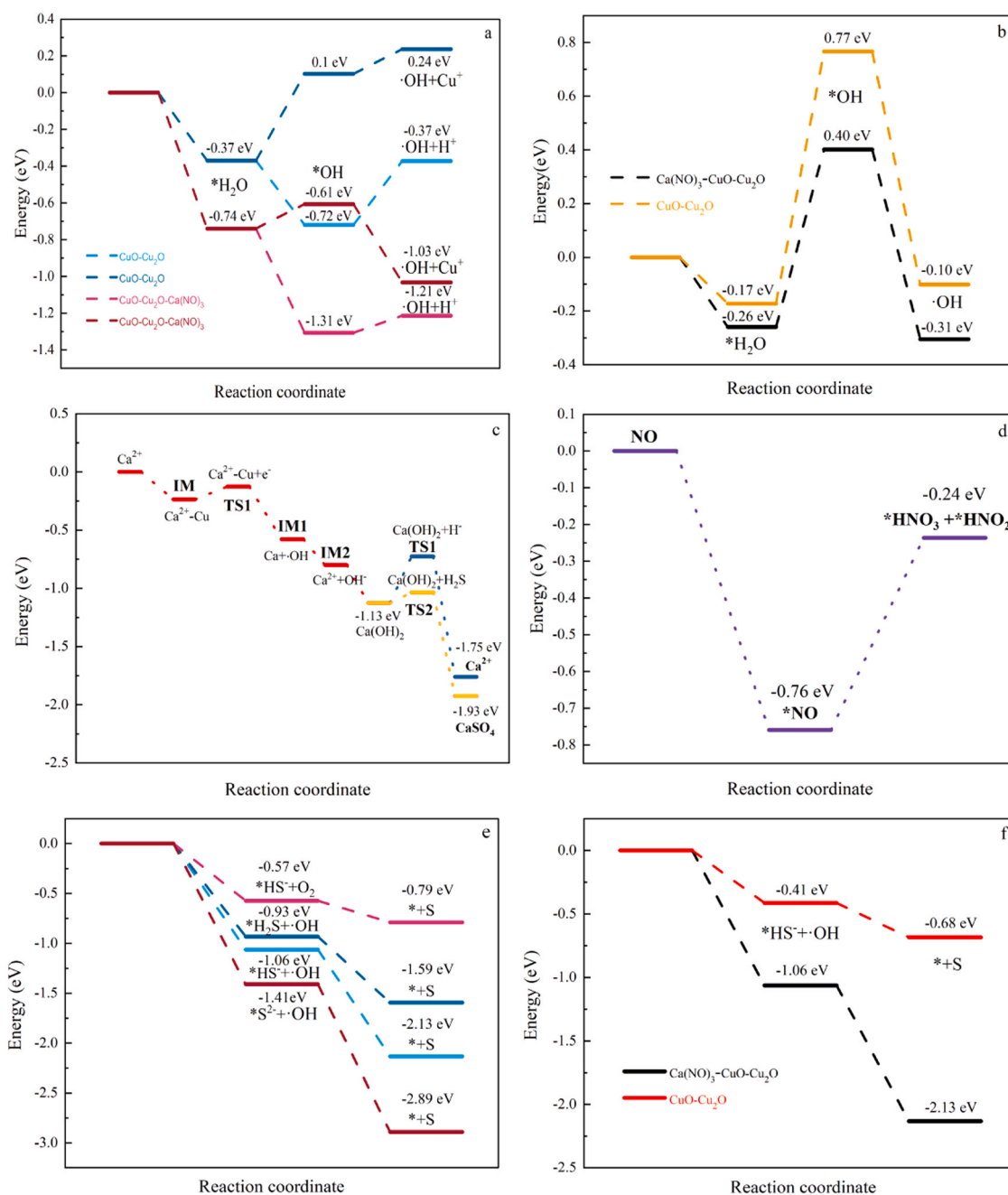
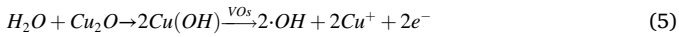
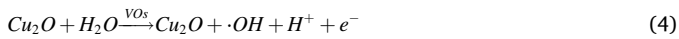


Fig. 8. Calculated energy profiles for adsorption and dissociation of H₂S over Cat_{Ca2.5Cu3} (a) Hydroxylation of H₂O by VOs (b), the reaction pathway of Ca²⁺ (c), NO cycle (d), H₂S/HS⁻ oxidation by O₂/·OH (e) over Cat_{Ca2.5Cu3}, and HS⁻ oxidation by ·OH of Ca(NO₃)₂-Cu₂O-CuO and Cu₂O-CuO (f).



Furthermore, CO₂-TPD results showed that the desulfurization performance of Cat_{Ca/Cu} was related to the concentration of VOs and the metal sites. Cu/Al₂O₃ catalyst significantly improved the H₂S desulfurization performance with the assistance of Ca(NO₃)₂, suggesting a synergistic catalytic effect between Cu_xO and Ca(NO₃)₂ that is connected with Ca(NO₃)₂. In the process of H₂S desulfurization, a large number of H⁺ are generated due to the dissociation of H₂S, which reduces the pH of the reaction system, and thus lowers the H₂S removal efficiency [75,76]. Additionally, free radicals are unstable and easily disrupted, leading to their conversion into oxygen and water, which cannot be effectively utilized. Therefore, we hypothesize that Ca²⁺ (basic site) acts as an intermediate to enrich ·OH and H⁺ ions. In this process, the basic site with some free radicals, delaying the ·OH quenching and slowing down the pH decrease, thereby decelerating the catalyst deactivation.

Additionally, the calculations also examined the reaction pathway of Ca²⁺ (Fig. 8c). The results showed that the Ca²⁺ generated by the dissociation of Ca(NO₃)₂ in the water film is initially spontaneously adsorbed on the surface of Cu (intermediate (IM), Fig. S14), then desorbs after adsorbing two e⁻ (TS1), and reacts with ·OH (IM1, (Fig. S15)) after electron exchange (IM2) to produce Ca(OH)₂ (Fig. S16). The heat energy of this reaction is -1.13 eV, respectively, indicating that the response is favorable thermodynamically. Ca(OH)₂ reacts with H⁺ present in the reaction system to produce Ca²⁺ (adsorption energy was -0.62 eV, Fig. 9).

The generated Ca²⁺ continues to participate in the cycle, facilitating the dissociation of H₂S and improving the utilization efficiency of ·OH. Furthermore, the calculation results show that the reaction between Ca(OH)₂ and H₂S to form CaSO₄ is also a spontaneous process (-0.8 eV), which would lead to the direct inactivation of Ca. This result is inconsistent with the experimental results, indicating that H₂S is initially captured and dissociated by the water film rather than directly contacting the active sites.

Furthermore, the NO₃⁻ can combine with H⁺ to produce strong oxidizing HNO₃ (Fig. S17) [77], which can oxidize HS⁻/S₂⁻ to form S and generate NO. Based on the experimental results, we hypothesize that this reaction is a cyclic process. Therefore, we calculated the probability of NO being captured by the water film in the presence of VOs. The calculation results show that the adsorption energy of NO being at VOs is -0.76 eV (Fig. 8d). The further reaction with H₂O to form HNO₃ and HNO₂ has the energy barrier and the heat of 0.52 eV and -0.24 eV, respectively. This confirms our hypothesis. During this process, the majority of HNO₂ is oxidized by oxygen to form HNO₃, while a small portion of oxidized H₂S forms S and generates N₂, which escapes and no longer participates in the cyclical reaction. This continues until all the N is converted to N₂ and escapes, at which point the reaction stops.

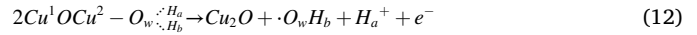
In addition to being hydroxylated by VO species, H₂O also serves the role of capturing and dissociating H₂S into H⁺, HS⁻, and S²⁻. The reaction

pathways of HS⁻ and S²⁻ were further calculated (Fig. 8e, f). The results indicate that ·OH oxidizes HS⁻ into adsorbed S more readily than O₂, and HS⁻/S²⁻ is more easily oxidized than H₂S (Fig. 8e). The generated S will desorb from the active site and migrate into the pores of the catalyst (Fig. S18). The adsorption energy of HS⁻ oxidized was reduced from -0.68 eV to -2.13 eV with the doping of Ca (Fig. 8f), indicating that adding Ca increases the catalytic oxidation efficiency of H₂S.

3.3.3. Desulfurization mechanisms

Based on the characterization analysis, experimental and DFT calculation results mentioned above, a rational reaction mechanism for H₂S desulfurization on Cat_{Ca2.5Cu3} in low temperature is proposed (Fig. 10).

First, a portion of H₂O in the gas mixture adsorbs on the catalyst surface through hydrogen bonding, forming a layer of water film. After being captured by the water film, H₂S dissolves and dissociates into H⁺ and HS⁻ (Eqs. 6–8). Another portion of H₂O adsorb on Cu_xO (active sites) (Eqs. 9–10), which are catalytically oxidized by VOs to form ·OH (Eqs. 11–12). Subsequently, a fraction of these radicals catalytically oxidizes HS⁻ and S²⁻ into S (Eqs. 13–14). Furthermore, S²⁻ and HS⁻ can also be directly oxidized to S by the adsorbed O₂ (Eqs. 15–16). This underlying mechanism allows Cat_{Cu3} to catalyze the oxidation of H₂S.



Although Ca/Al₂O₃ cannot directly utilize H₂O at low temperatures, the primary sites provided by Ca²⁺ (obtained by Eq. 17) can accumulate the electrons generated in the above reaction, forming a high-density electron cloud (Eq. 18). This attracts the enrichment of ·OH on Ca, forming a stable intermediate Ca(OH)₂ (Eq. 19), which then reacts with H⁺ in the reaction system (Eq. 20) to promote the dissociation of H₂S (Eqs. 6–7) and the generation of ·OH (Eq. 11).

NO₃⁻ can react with H⁺ to form a strong oxidant, HNO₃, which directly oxidizes HS⁻/S²⁻ to S (Eqs. 21–22). NO, produced as a reaction product, can be captured by VOs and further reacts with H₂O to generate HNO₃ and HNO₂ (Eq. 23), which continue to react with HS⁻/S²⁻. Most of the HNO₂ will be oxidized to HNO₃ by the adsorbed O₂ (Eq. 24). N₂ from HNO₂ and HS⁻/S²⁻ reaction will continuously overflow without further reactions (Eq. 25). This reaction will cycle until all the N overflows. Therefore, the presence of Ca(NO₃)₂ can effectively improve the utilization rate of ·OH and continuously consume H₂S, thus accelerating the catalytic rate.

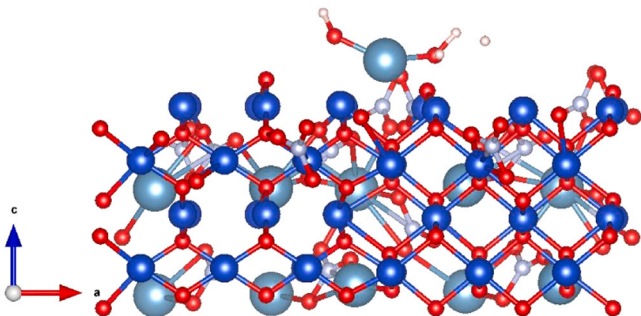


Fig. 9. Adsorption configuration diagram of Ca(OH)₂ adsorb H⁺.

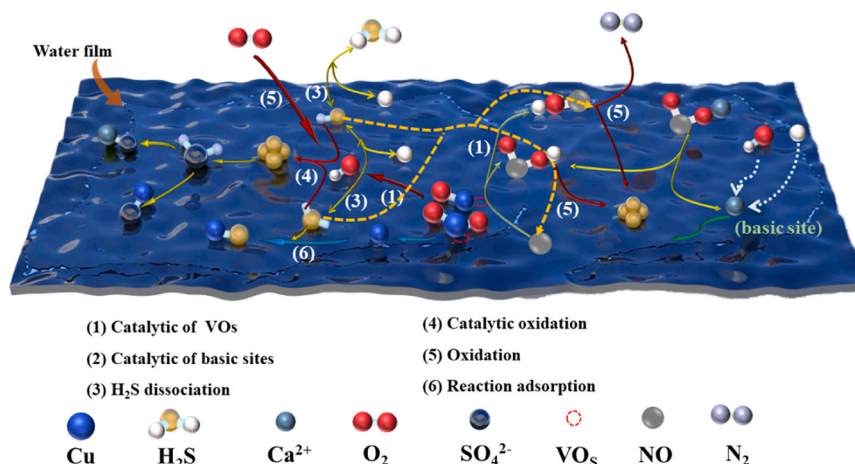
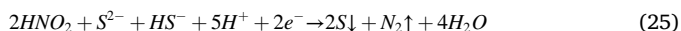
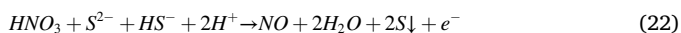
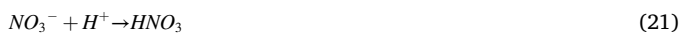
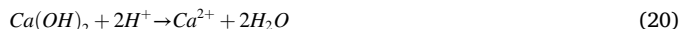
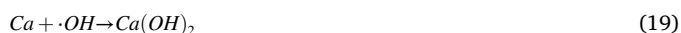


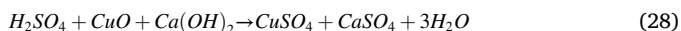
Fig. 10. The proposed desulfurization mechanism of Cat_{Ca2.5Cu3}.



During the reaction process, S^{2-} will react with Cu^{2+} to generate CuS.



Eventually, the produced S undergoes further oxidation through adsorbed oxygen and concurrently reacts with H_2O to form H_2SO_4 (Eq. 27). As the H_2SO_4 reacted with CuO and $\text{Ca}(\text{OH})_2$, sulfate was formed (Eq. 28). Gradually, desulfurization came to a halt due to active centers disappearing, and sulfur and sulfate accumulation.



In summary, the VOx provided by Cu_xO are essential for the low-temperature removal of H_2S . The synergistic interaction between VOx and $\text{Ca}(\text{NO}_3)_2$ is the fundamental reason behind the excellent catalytic performance of Cat_{Ca2.5Cu3} at low temperatures.

3.4. Sulfur recovery

The generation of sulfur salts and sulfides is approximately equal to the theoretical sulfur capacity, and the production of S is estimated by subtracting the theoretical sulfur capacity from the measured sulfur capacity. Approximately 0.34 g of S was adsorbed in the pores of 1 g Cat_{Ca2.5Cu3} spent catalyst (Sulfur selectivity > 90%). Sulfur recovery experiments were conducted at temperatures above the sulfur dew point to enhance economic benefits. Approximately 0.31 g of sulfur was obtained as a recovery from 1 g of catalyst (Fig. S19). The resource recovery reduces the cost of H_2S removal and improves the sulfur yield.

4. Conclusions

In conclusion, a series of Ca-Cu_xO/Al₂O₃ were successfully

synthesized by the excessive impregnation method and used for H_2S removal at a low temperature. Optimize the Ca content, reaction temperature, and humidity by H_2S dynamic removal experiments; the experiments results showed that the Ca-Cu_xO/Al₂O₃ catalyst with 2.5 wt% Ca has the best H_2S removal capacity at 60 °C and RH 60%, reaching 401.34 mg H_2S /g catalyst. H_2O plays a vital role in the catalytic oxidation of H_2S : the catalytic oxidation does not occur without H_2O . The XPS, TG, and TEM characterizations exhibited that the active components of the catalyst were $\text{Ca}(\text{NO}_3)_2$, Cu₂O, and CuO, which interlaced to form nanosheets, thereby increasing the contact area with H_2S . Moreover, the XPS, EPR, FTIR, and CO₂-TPD characterizations demonstrated that the Ca-Cu_xO/Al₂O₃ catalyst possesses abundant VOx and basic sites. The H_2S removal performance was strongly correlated with the sum of moderate-basicity sites (i.e., VOx) and strong-basicity sites (i.e., metallic sites), which collectively promote the generation of $\cdot\text{OH}$. In addition, although Ca/Al₂O₃ has many basic sites, it lacks VOx, resulting in no generation of $\cdot\text{OH}$ and no catalytic effect on H_2S . This signifies that VOx serve as the foundation for the generation of $\cdot\text{OH}$, which in turn is the basis for the catalytic oxidation of H_2S . Furthermore, the XPS characterization of Cat_{Ca2.5Cu3} exhibited the H_2S desulfurization products were CaSO₄, CuSO₄, CuS, and S. According to the experiment, characterization, and DFT results, a mechanism of H_2S removal is proposed, which involves physical adsorption, chemical adsorption, and catalytic oxidation. The catalytic oxidation of sulfide anions by $\cdot\text{OH}$ produced via hydroxylation of H_2O by VOx is not the only mechanism involved. The redundant $\cdot\text{OH}$ adsorbed on the basic sites on the catalyst surface can buffer the pH and promote the dissociation of H_2S . In addition, the NO₃ species reacted with H^+ to oxidize the anionic sulfur species. The above cyclic process could alleviate the deactivation of the Ca-Cu/Al₂O₃ catalyst. Furthermore, we have also found that the catalyst deactivates before fully utilizing the pore volume. Sulfur recovery from the spent catalysts was possible after the reaction. This suggests that there is potential for further modification and design of the catalyst's active sites to achieve higher H_2S removal capacity.

CRediT authorship contribution statement

Mengxue Yin: Writing – original draft, Validation, Investigation, Formal analysis. **Hailong Wang:** Validation, Investigation. **Wenqing Zhang:** Writing – original draft, Formal analysis. **Yan Zheng:** Writing – review & editing. **Long Zhao:** Validation. **Feiyue Fan:** Writing – review & editing, Conceptualization. **H. Hou:** Writing – review & editing, Resources, Project administration. **Suresh C. Pillai:** Writing – review & editing. **Hongliang Yin:** Investigation. **Zhihao Wu:** Validation.

Declaration of Competing Interest

The authors declare that they have no known competing financial interests or personal relationships that could have appeared to influence the work reported in this paper.

Data Availability

No data was used for the research described in the article.

Acknowledgements

This work was supported by National Key Research and Development Program [Grant No. 2020YFC1807700], and the Guangdong Foundation for Program of Science and Technology Research, China (Grant No. 2023B1212060044).

Appendix A. Supporting information

Supplementary data associated with this article can be found in the online version at [doi:10.1016/j.apcatb.2024.123981](https://doi.org/10.1016/j.apcatb.2024.123981).

References

- [1] L. Li, T.H. Sun, C.H. Shu, H.B. Zhang, Low temperature H₂S removal with 3-D structural mesoporous molecular sieves supported ZnO from gas stream, *J. Hazard. Mater.* 311 (2016) 142–150, <https://doi.org/10.1016/j.jhazmat.2016.01.033>.
- [2] G. Jiang, D. Melder, J. Keller, Z. Yuan, Odor emissions from domestic wastewater: a review, *Crit. Rev. Environ. Sci. Tec.* 47 (2017) 1581–1611, <https://doi.org/10.1080/10643389.2017.1386952>.
- [3] S. Lee, D. Kim, Enhanced adsorptive removal of hydrogen sulfide from gas stream with zinc-iron hydroxide at room temperature, *Chem. Eng. J.* 363 (2019) 43–48, <https://doi.org/10.1016/j.cej.2019.01.122>.
- [4] R. Zhang, H. Liu, J. Li, L. Ling, B. Wang, A mechanistic study of H₂S adsorption and dissociation on Cu₂O (111) surfaces: Thermochemistry, reaction barrier, *Appl. Surf. Sci.* 258 (2012) 9932–9943, <https://doi.org/10.1016/j.apsusc.2012.06.053>.
- [5] J. Wang, L.J. Wang, H.L. Fan, H. Wang, Y.F. Hu, Z.D. Wang, Highly porous copper oxide sorbent for H₂S capture at ambient temperature, *Fuel* 209 (2017) 329–338, <https://doi.org/10.1016/j.fuel.2017.08.003>.
- [6] A. PiéPlu, O. Saur, J.-C. Lavalley, O. Legendre, C. Nédéz, Claus Catalysis and H₂S Selective Oxidation, *Catal. Rev.* 40 (1998) 409–450, <https://doi.org/10.1080/01614949808007113>.
- [7] X. Zhang, Y. Tang, S. Qu, J. Da, Z. Hao, H₂S-selective catalytic oxidation: catalysts and processes, *ACS Catal.* 5 (2015) 1053–1067, <https://doi.org/10.1021/cs501476p>.
- [8] S. Ibrahim, A. Al Shoaibi, A.K. Gupta, Toluene destruction in thermal stage of Claus reactor with oxygen enriched air, *Appl. Energ.* 115 (2014) 1–8, <https://doi.org/10.1016/j.apenergy.2013.10.060>.
- [9] R.A. Pandey, S. Malhotra, Desulfurization of gaseous fuels with recovery of elemental sulfur: an overview, *Crit. Rev. Environ. Sci. Tec.* 29 (1999) 229–268, <https://doi.org/10.1080/10643389991259236>.
- [10] C. Yang, Y. Wang, M. Liang, Z. Su, X. Liu, H. Fan, T.J. Bandoz, Towards improving H₂S catalytic oxidation on porous carbon materials at room temperature: A review of governing and influencing factors, recent advances, mechanisms and perspectives, *Appl. Catal. B-Environ.* 323 (2023), <https://doi.org/10.1016/j.apcatb.2022.122133>.
- [11] S. Liang, F. Liu, L. Jiang, Recent advances on nitrogen-doped metal-free materials for the selective catalytic oxidation of hydrogen sulfide, *Curr. Opin. Green. Sust.* 25 (2020), <https://doi.org/10.1016/j.cogsc.2020.100361>.
- [12] M. Xue, R. Chitrakar, K. Sakane, K. Ooi, Screening of adsorbents for removal of H₂S at room temperature, *Green. Chem.* 5 (2003) 529–534, <https://doi.org/10.1039/b303167p>.
- [13] T. Raabe, M. Mehne, H. Rasser, H. Krause, S. Kureti, Study on iron-based adsorbents for alternating removal of H₂S and O₂ from natural gas and biogas, *Chem. Eng. J.* 371 (2019) 738–749, <https://doi.org/10.1016/j.cej.2019.04.103>.
- [14] L. Neveux, D. Chiche, D. Bazer-Bachi, L. Favregeon, M. Pijolat, New insight on the ZnO sulfidation reaction: Evidences for an outward growth process of the ZnS phase, *Chem. Eng. J.* 181–182 (2012) 508–515, <https://doi.org/10.1016/j.cej.2011.09.019>.
- [15] N.K. Gupta, J. Bae, K.S. Kim, A novel one-step synthesis of Ce/Mn/Fe mixed metal oxide nanocomposites for oxidative removal of hydrogen sulfide at room temperature, *RSC Adv.* 11 (2021) 26739–26749, <https://doi.org/10.1039/d1ra03309c>.
- [16] T. Baird, K.C. Campbell, P.J. Holliman, R.W. Hoyle, M. Huxam, D. Stirling, B. P. Williams, M. Morris, Cobalt-zinc oxide adsorbents for low temperature gas desulfurisation, *J. Mater. Chem.* 9 (1999) 599–605, <https://doi.org/10.1039/A806909C>.
- [17] P. Dhage, A. Samokhvalov, D. Repala, E.C. Duin, B.J. Tatarchuk, Regenerable Fe-Mn-ZnO/SiO₂ sorbents for room temperature removal of H₂S from fuel reformates: performance, active sites, Operando studies, *Phys. Chem. Chem. Phys.* 13 (2011) 2179–2187, <https://doi.org/10.1039/c0cp01355b>.
- [18] C. Yang, S. Yang, H.L. Fan, J. Wang, H. Wang, J. Shangguan, C. Huo, A sustainable design of ZnO-based adsorbent for robust H₂S uptake and secondary utilization as hydrogenation catalyst, *Chem. Eng. J.* 382 (2020), <https://doi.org/10.1016/j.cej.2019.122892>.
- [19] H. Yang, B. Tatarchuk, Novel-doped zinc oxide sorbents for low temperature regenerable desulfurization applications, *AIChE J.* 56 (2010) 2898–2904, <https://doi.org/10.1002/aic.12201>.
- [20] P. Dhage, A. Samokhvalov, D. Repala, E.C. Duin, M. Bowman, B.J. Tatarchuk, Copper-Promoted ZnO/SiO₂ Regenerable Sorbents for the Room Temperature Removal of H₂S from Reformate Gas Streams, *Ind. Eng. Chem. Res.* 49 (2010) 8388–8396, <https://doi.org/10.1021/ie100209a>.
- [21] M. Yan, W. Fang, H. Feng, Y. Zhang, H. Wibowo, E. Kanchanatip, D.A. Rahim, Performance evaluation of Zn-Fe adsorbent for H₂S adsorption during biogas purification, *Biomass-Conv. Bior.* (2022) 1–11, <https://doi.org/10.1007/s13399-022-02959-3>.
- [22] A. Daneshyar, M. Ghaedi, M.M. Sabzehmeidani, A. Daneshyar, H₂S adsorption onto Cu-Zn-Ni nanoparticles loaded activated carbon and Ni-Co nanoparticles loaded gamma-Al₂O₃: Optimization and adsorption isotherms, *J. Colloid Interface Sci.* 490 (2017) 553–561, <https://doi.org/10.1016/j.jcis.2016.11.068>.
- [23] M.X. Yin, Z.C. Yun, F.Y. Fan, S.C. Pillai, Z.H. Wu, Y. Zheng, L. Zhao, H.L. Wang, H. Hou, Insights into the mechanism of low-temperature H₂S oxidation over Zn-Cu/Al₂O₃ catalyst, *Chemosphere* (2021) 133105, <https://doi.org/10.1016/j.chemosphere.2021.133105>.
- [24] X. Wang, J.K. Chong, S.Y. Liang, M. Guo, M. Zhang, Contributions of Mn-doping in CuO/Al₂O₃ sorbent for enhancement of H₂S removal at low and wide temperature range, *Fuel* 334 (2023) 126546, <https://doi.org/10.1016/j.fuel.2022.126546>.
- [25] Z. Zhang, J. Wang, W. Li, M. Wang, W. Qiao, D. Long, L. Ling, Millimeter-sized mesoporous carbon spheres for highly efficient catalytic oxidation of hydrogen sulfide at room temperature, *Carbon* 96 (2016) 608–615, <https://doi.org/10.1016/j.carbon.2015.10.001>.
- [26] Z. Zhang, W. Jiang, D. Long, J. Wang, W. Qiao, L. Ling, A General Silica-Templating Synthesis of Alkaline Mesoporous Carbon Catalysts for Highly Efficient H₂S Oxidation at Room Temperature, *ACS Appl. Mater. Inter.* 9 (2017) 2477–2484, <https://doi.org/10.1021/acsami.6b13597>.
- [27] Q. Chen, J. Wang, X. Liu, X. Zhao, W. Qiao, D. Long, L. Ling, Alkaline carbon nanotubes as effective catalysts for H₂S oxidation, *Carbon* 49 (2011) 3773–3780, <https://doi.org/10.1016/j.carbon.2011.05.011>.
- [28] Y. Li, H. Qi, C. You, X. Xu, Kinetic model of CaO/fly ash sorbent for flue gas desulfurization at moderate temperatures, *Fuel* 86 (2007) 785–792, <https://doi.org/10.1016/j.fuel.2006.09.011>.
- [29] Y. Pan, M. Chen, Z. Su, K. Wu, Y. Zhang, D. Long, Two-dimensional CaO/carbon heterostructures with unprecedented catalytic performance in room-temperature H₂S oxidation, *Appl. Catal. B-Environ.* 280 (2021) 119444, <https://doi.org/10.1016/j.apcatb.2020.119444>.
- [30] Y. Yuan, L.J. Huang, T.C. Zhang, Y. Wang, S.J. Yuan, CaCO₃-ZnO loaded scrap rice-derived biochar for H₂S removal at room-temperature: Characterization, performance and mechanism, *Fuel Process. Technol.* 249 (2023) 107846, <https://doi.org/10.1016/j.fuproc.2023.107846>.
- [31] G.G. Kresse, J.J. Furthmüller, Efficient iterative schemes for ab initio total-energy calculations using a plane-wave basis set, *Phys. Rev. B* 54 (1996) 11169–11186, <https://doi.org/10.1103/PhysRevB.54.11169>.
- [32] J.P. Perdew, K. Burke, M. Ernzerhof, Generalized Gradient Approximation Made Simple, *Phys. Rev. Lett.* 77 (1996) 3865–3869, <https://doi.org/10.1103/PhysRevLett.77.3865>.
- [33] P.E. Blochl, Projector augmented-wave method, *Phys. Rev. B Condens. Matter* 50 (1994) 17953–17979, <https://doi.org/10.1103/physrevb.50.17953>.
- [34] G. Kresse, D. Joubert, From ultrasoft pseudopotentials to the projector augmented-wave method, *Phys. Rev. B* 59 (1999) 1758–1775, <https://doi.org/10.1103/PhysRevB.59.1758>.
- [35] S. Grimme, J. Antony, S. Ehrlich, H. Krieg, A consistent and accurate ab initio parametrization of density functional dispersion correction (DFT-D) for the 94 elements H-Pu, *J. Chem. Phys.* 132 (2010) 154104, <https://doi.org/10.1063/1.3382344>.
- [36] G. Leofanti, M. Padovan, G. Tozzola, B. Venturelli, Surface area and pore texture of catalysts, *Catal. Today* 41 (1998) 207–219, [https://doi.org/10.1016/S0920-5861\(98\)00050-9](https://doi.org/10.1016/S0920-5861(98)00050-9).
- [37] X. Zhang, Z. Wang, N. Qiao, S. Qu, Z. Hao, Selective catalytic oxidation of H₂S over well-mixed oxides derived from Mg₂Al₂X₃-x layered double hydroxides, *ACS Catal.* 4 (2014) 1500–1510, <https://doi.org/10.1021/cs500303y>.
- [38] T.J. Bandoz, On the adsorption/oxidation of hydrogen sulfide on activated carbons at ambient temperatures, *J. Colloid Interface Sci.* 246 (2002) 1–20, <https://doi.org/10.1006/jcis.2001.7952>.
- [39] H.L. Zhu, D. Papurello, M. Gandiglio, A. Lanzini, I. Akinlar, P.R. Shearing, G. Manos, D.J.L. Brett, Y.S. Zhang, Study of H₂S removal capability from simulated biogas by using waste-derived adsorbent materials, *Processes* 8 (2020) 1030, <https://doi.org/10.3390/pr8091030>.
- [40] B. Demri, D. Muster, XPS study of some calcium compounds, *J. Mater. Process. Tech.* 55 (1995) 311–314, [https://doi.org/10.1016/0924-6460\(95\)02023-3](https://doi.org/10.1016/0924-6460(95)02023-3).
- [41] Y. Fan, Y. Zhuo, L. Li, SeO₂ adsorption on CaO surface: DFT and experimental study on the adsorption of multiple SeO₂ molecules, *Appl. Surf. Sci.* 420 (2017) 465–471, <https://doi.org/10.1016/j.apsusc.2017.04.233>.
- [42] W.J. Lee, Y.S. Lee, S.K. Rha, Y.J. Lee, K.Y. Lim, Y.D. Chung, C.N. Whang, Adhesion and interface chemical reactions of Cu/polyimide and Cu/TiN by XPS, *Appl. Surf. Sci.* 205 (2003) 128–136, [https://doi.org/10.1016/S0169-4332\(02\)01016-4](https://doi.org/10.1016/S0169-4332(02)01016-4).

- [43] D. Chalasani, J. Li, N.M. Jackson, M. Payne, B.L. Lucht, Methylene ethylene carbonate: novel additive to improve the high temperature performance of lithium ion batteries, *J. Power Sources* 208 (2012) 67–73, <https://doi.org/10.1016/j.jpowsour.2012.02.004>.
- [44] I. Matsushita, T. Suzuki, T. Moriga, T. Ashida, I. Nakabayashi, J. Metson, XPS study on the carbonation process of $\text{Ca}(\text{OH})_2$, *J. Ceram. Soc. Jpn.* 101 (1993) 725–727, <https://doi.org/10.2109/jcersj.101.725>.
- [45] K. Kukli, M. Ritala, T. Sajavaara, T. Hänninen, M. Leskelä, Atomic layer deposition of calcium oxide and calcium hafnium oxide films using calcium cyclopentadienyl precursor, *Thin Solid Films* 500 (2006) 322–329, <https://doi.org/10.1016/j.tsf.2005.10.082>.
- [46] D. Gao, G. Yang, J. Li, J. Zhang, J. Zhang, D. Xue, Room-Temperature Ferromagnetism of Flowerlike CuO Nanostructures, *J. Phys. Chem. C* 114 (2010) 18347–18351, <https://doi.org/10.1021/jp106015t>.
- [47] X. Ma, X. Feng, J. Guo, H. Cao, X. Suo, H. Sun, M. Zheng, Catalytic oxidation of 1,2-dichlorobenzene over Ca -doped FeOx hollow microspheres, *Appl. Catal. B-Environ.* 147 (2014) 666–676, <https://doi.org/10.1016/j.apcatb.2013.10.003>.
- [48] C. Yang, J. Wang, H.L. Fan, J. Shangguan, J. Mi, C. Huo, Contributions of tailored oxygen vacancies in $\text{ZnO}/\text{Al}_2\text{O}_3$ composites to the enhanced ability for H_2S removal at room temperature, *Fuel* 215 (2018) 695–703, <https://doi.org/10.1016/j.fuel.2017.11.037>.
- [49] X. Zheng, Y. Li, W. You, G. Lei, Y. Cao, Y. Zhang, L. Jiang, Construction of Fe -doped TiO_2 -x ultrathin nanosheets with rich oxygen vacancies for highly efficient oxidation of H_2S , *Chem. Eng. J.* 430 (2022) 132917, <https://doi.org/10.1016/j.cej.2021.132917>.
- [50] X. Zheng, B. Li, L. Shen, Y. Cao, Y. Zhan, S. Zheng, S. Wang, L. Jiang, Oxygen vacancies engineering of Fe doped LaCoO_3 perovskite catalysts for efficient H_2S selective oxidation, *Appl. Catal. B: Environ.* 329 (2023) 122526, <https://doi.org/10.1016/j.apcatb.2023.122526>.
- [51] N. Shahzad, A. Hussain, N. Mustafa, N. Ali, M.B. Kanoun, S. Goumri-Said, First principles study of the adsorption and dissociation mechanisms of H_2S on a TiO_2 anatase (001) surface, *RSC Adv.* 6 (2016) 7941–7949, <https://doi.org/10.1039/c5ra20875k>.
- [52] T. Ghodselahe, M.A. Vesaghi, A. Shafiekhani, A. Baghizadeh, M. Lameii, XPS study of the $\text{Cu}@/\text{Cu}_2\text{O}$ core-shell nanoparticles, *Appl. Surf. Sci.* 255 (2008) 2730–2734, <https://doi.org/10.1016/j.apsusc.2008.08.110>.
- [53] Z.S. Li, T. Liu, Y. Sun, S. Deng, Y. Li, Y. Tan, Z. Ma, H. Zhang, Well-dispersed Cu Fe doping nanoparticles with mixed valence in carbon aerogel as effective adsorbent for H_2S removal at low temperature, *Fuel Process. Technol.* 245 (2023) 107744, <https://doi.org/10.1016/j.fuproc.2023.107744>.
- [54] J. Cr  pelli  re, P.L. Popa, N. Bahlawane, R. Leturcq, F. Werner, S. Siebentritt, D. Lenoble, Transparent conductive CuCrO_2 thin films deposited by pulsed injection metal organic chemical vapor deposition: up-scalable process technology for an improved transparency/conductivity trade-off, *J. Mater. Chem. C* 4 (2016) 4278–4287, <https://doi.org/10.1039/c6tc00383d>.
- [55] N. Jiang, H. Sun, D. Ren, Q. Pang, F. Jin, Z. Huo, A structure-activity controllable synthesis of skeletal CuAlZn catalyst for hydrogenation of bicarbonate to formic acid in water, *J. CO₂ Util.* 20 (2017) 218–223, <https://doi.org/10.1016/j.jcou.2017.05.015>.
- [56] D. Li, S. Zuo, H. Xu, J. Zan, L. Sun, D. Han, W. Liao, B. Zhang, D. Xia, Synthesis of a $\text{g-C}_3\text{N}_4\text{-Cu}_2\text{O}$ heterojunction with enhanced visible light photocatalytic activity by PEG, *J. Colloid Interface Sci.* 531 (2018) 28–36, <https://doi.org/10.1016/j.jcis.2018.07.018>.
- [57] Y. Wang, X. Liu, M. Duan, C. Zhang, H. Fan, C. Yang, T. Jiao, T. Kou, J. Shangguan, Synergistic effect of bimetal in isorecticular $\text{Zn-Cu-1,3,5-benzenetricarboxylate}$ on room temperature gaseous sulfides removal, *J. Colloid Interface Sci.* 641 (2023) 707–718, <https://doi.org/10.1016/j.jcis.2023.03.108>.
- [58] X. Li, X. Wang, L. Yuan, L. Wang, Y. Ma, Y. Wu, Y. Xie, R. Cao, Y. Xiong, P. Ning, COS and H_2S simultaneous removal from blast furnace gas over a tailored Cu/Zr co-doped K@TiO_2 bifunctional catalyst under low temperature, *Chem. Eng. J.* 471 (2023) 144573, <https://doi.org/10.1016/j.cej.2023.144573>.
- [59] R. Katal, S. Masudy-Panah, M. Sabbaghian, Z. Hossaini, M.H. Davood Abadi Farahani, Photocatalytic degradation of triclosan by oxygen defected CuO thin film, *Sep. Purif. Technol.* 250 (2020) 250, <https://doi.org/10.1016/j.seppur.2020.117239>.
- [60] M. Bailera, P. Lisbona, L.M. Romeo, S. Espatolero, Power to Gas projects review: lab, pilot and demo plants for storing renewable energy and CO_2 , *Renew. Sust. Energy Rev.* 69 (2017) 292–312, <https://doi.org/10.1016/j.rser.2016.11.130>.
- [61] X. Song, D. Pan, Y. Wu, P. Cheng, R. Wei, L. Gao, J. Zhang, G. Xiao, Synthesis of glycerol carbonate over porous La-Zr based catalysts: The role of strong and super basic sites, *J. Alloy. Compd.* 750 (2018) 828–837, <https://doi.org/10.1016/j.jallcom.2018.03.392>.
- [62] Y. Pan, H. Xu, M. Chen, K. Wu, Y. Zhang, D. Long, Unveiling the Nature of Room-Temperature O_2 Activation and O_2^- Enrichment on MgO -loaded porous carbons with efficient H_2S oxidation, *ACS Catal.* 11 (2021) 5974–5983, <https://doi.org/10.1021/acscatal.1c00857>.
- [63] J. Wang, B. Li, Y. Li, X. Fan, F. Zhang, G. Zhang, Y. Zhu, W. Peng, Easily regenerated $\text{CuO}/\gamma\text{-Al}_2\text{O}_3$ for persulfate-based catalytic oxidation: insights into the deactivation and regeneration mechanism, *ACS Appl. Mater. Interfaces* 13 (2021) 2630–2641, <https://doi.org/10.1021/acsaami.0c19013>.
- [64] M.M. Roessler, E. Salvadori, Principles and applications of EPR spectroscopy in the chemical sciences, *Chem. Soc. Rev.* 47 (2018) 2534–2553, <https://doi.org/10.1039/c6cs00565a>.
- [65] G. Liu, T. Schultze, J. Br  tz, A. Klein, W. Jaegermann, Interface properties and band alignment of $\text{Cu}_2\text{S}/\text{CdS}$ thin film solar cells, *Thin Solid Films* 431–432 (2003) 477–482, [https://doi.org/10.1016/s0040-6090\(03\)00190-1](https://doi.org/10.1016/s0040-6090(03)00190-1).
- [66] L. Yang, Y. Yao, G. Zhu, M. Ma, W. Wang, L. Wang, H. Zhang, Y. Zhang, Z. Jiao, Co doping of worm-like Cu_2S : an efficient and durable heterogeneous electrocatalyst for alkaline water oxidation, *J. Alloy. Compd.* 762 (2018) 637–642, <https://doi.org/10.1016/j.jallcom.2018.05.249>.
- [67] X. Dai, L. Chen, Z. Li, X. Li, J. Wang, X. Hu, L. Zhao, Y. Jia, S.X. Sun, Y. Wu, Y. He, $\text{CuS}/\text{KTA}_{0.75}\text{Nb}_{0.25}\text{O}_3$ nanocomposite utilizing solar and mechanical energy for catalytic N_2 fixation, *J. Colloid Interface Sci.* 603 (2021) 220–232, <https://doi.org/10.1016/j.jcis.2021.06.107>.
- [68] C. Yang, G. de Falco, M. Florent, H. Fan, M. Liang, T.J. Bandoz, The effect of ZnFe_2O_4 /activated carbon adsorbent photocatalytic activity on gas-phase desulfurization, *Chem. Eng. J.* 423 (2021) 130255, <https://doi.org/10.1016/j.cej.2021.130255>.
- [69] J. Huang, T. Huang, H. Chunluan, W. Huang, R.X. Ma, The Function of Sb_{15} -over $\text{Ni}/\text{Mo}_2\text{C}$ Catalysts for Carbon Dioxide Reforming of Methane, *Adv. Mater. Res.* 455–456 (2012) 174–179, <https://doi.org/10.4028/www.scientific.net/AMR.455-456.174>.
- [70] N. Karikalan, R. Karthik, S.M. Chen, C. Karupiah, A. Elangovan, Sonochemical synthesis of sulfur doped reduced graphene oxide supported CuS nanoparticles for the non-enzymatic glucose sensor applications, *Sci. Rep.* 7 (2017) 2494, <https://doi.org/10.1038/s41598-017-02479-5>.
- [71] J.R. Vegelius, K.O. Kvashnina, H. Hollmark, M. Klintonberg, Y.O. Kvashnin, I. L. Soroka, L. Werme, S.M. Butorin, X-ray spectroscopic study of Cu_2S , CuS , and copper films exposed to Na_2S Solutions, *J. Phys. Chem. C* 116 (2012) 22293–22300, <https://doi.org/10.1021/jp302390c>.
- [72] J.C. Klein, A. Proctor, D.M. Hercules, J.F. Black, X-ray excited auger intensity ratios for differentiating copper compounds, *Anal. Chem.* 55 (1983) 2055–2059, <https://doi.org/10.1021/ac00263a011>.
- [73] H.F. Franzen, J. Merrick, M. Umana, A.S. Khan, D.T. Peterson, J.R. McCreary, R. J. Thorn, XPS spectra and crystalline potentials in alkaline-earth chalcogenides and hydrides, *J. Electron Spectrosc. Relat. Phenom.* 11 (1977) 439–443, [https://doi.org/10.1016/0368-2048\(77\)80019-4](https://doi.org/10.1016/0368-2048(77)80019-4).
- [74] A.B. Christie, J. Lee, I. Sutherland, J.M. Walls, An XPS study of ion-induced compositional changes with group II and group IV compounds, *Appl. Surf. Sci.* 15 (1983) 224–237, [https://doi.org/10.1016/0378-5963\(83\)90018-1](https://doi.org/10.1016/0378-5963(83)90018-1).
- [75] F. Adib, A. Bagreev, T.J. Bandoz, Effect of surface characteristics of wood-based activated carbons on adsorption of hydrogen sulfide, *J. Colloid Interface Sci.* 214 (1999) 407–415, <https://doi.org/10.1006/jcis.1999.6200>.
- [76] A.B. Foad Adib, Teresa J. Bandoz, Effect of pH and surface chemistry on the mechanism of H_2S removal by activated carbons, *J. Colloid Interface Sci.* 216 (1999) 360–369, <https://doi.org/10.1006/jcis.1999.6335>.
- [77] D. Barrera, F.G. de Mendon  a, A.H. de Castro, J.P. de Mesquita, R.M. Lago, K. Sapag, Surface modified mesoporous nanocast carbon as a catalyst for aqueous sulfide oxidation and adsorption of the produced polysulfides, *N. J. Chem.* 42 (2018) 11708–11714, <https://doi.org/10.1039/c8nj00922h>.